Summer 8-20-2021

The Effect of Non-Local Electrical Conductivity on Near-Field Radiative Heat Transfer Between Graphene Sheets

Behrad Zeinali Tajani
University of Maine, behrad.zeinali@maine.edu

THE EFFECT OF NON-LOCAL ELECTRICAL CONDUCTIVITY ON NEAR-FIELD RADIATIVE HEAT TRANSFER BETWEEN GRAPHENE SHEETS

By

Behrad Zeinali Tajani

M.Sc. in Mechanical Engineering, University of Zanjan, 2017

A THESIS

Submitted in Partial Fulfillment of the

Requirements for the Degree of

Master of Science

(in Mechanical Engineering)

The Graduate School

The University of Maine

August 2021

Advisory Committee:

Dr. Sheila Edalatpour, Assistant Professor of Mechanical Engineering, Advisor

Dr. Yingchao Yang, Assistant Professor of Mechanical Engineering

Dr. Olivier Putzeys, Lecturer of Mechanical Engineering

THE EFFECT OF NON-LOCAL ELECTRICAL CONDUCTIVITY ON NEAR-FIELD RADIATIVE HEAT TRANSFER BETWEEN GRAPHENE SHEETS

By Behrad Zeinali Tajani

Thesis Advisor: Dr. Sheila Edalatpour

An Abstract of the Thesis Presented
in Partial Fulfillment of the Requirements for the
Degree of Master of Science
(in Mechanical Engineering)
August 2021

Every object above zero kelvin emits electromagnetic radiation with the dominant wavelength determined using the Wien's law (10 microns at room temperature). These waves can transfer energy and hence are the foundation of radiative heat transfer (RHT). RHT consists of two regimes: far-field and near-field. If the distance between the heat exchanging media is more than the dominant wavelength, the regime is far-field and is limited to the ideal Planck's blackbody, and only propagating waves contribute to heat transfer. On the other hand, when the distance is less than the dominant wavelength, the regime is called the near-field. In near-field radiative heat transfer (NFRHT), the contribution of evanescent waves becomes more significant than the propagating ones, and this causes a spike in the spectral RHT that exceeds Planck's blackbody limit by several orders of magnitude. If the thermal emitter supports surface modes, NFRHT can become monochromatic.

These surface modes can be surface phonon polaritons (SPhP) and surface plasmon polaritons (SPP). Materials such as silicon carbide support SPhP and graphene is an example of a material that support SPPs. These surface modes cause the quasi-monochromatic behavior that can be exploited for applications such as

thermophotovoltaic devices and thermal rectifiers. Graphene is one of the few materials that support surface modes in the infrared where these modes can be thermally excited. Another characteristic of graphene SPPs is their tunability using gate voltage or chemical doping which has transformed graphene into a revolutionary material for NFRHT applications in mid-to far-infrared regions.

Graphene has been studied both theoretically and experimentally. However, in most NFRHT studies, graphene has been investigated theoretically for its application in NFRHT. NFRHT for graphene is calculated using its electrical conductivity. The studies in NFRHT have utilized a local method for graphene's electrical conductivity called the Kubo formula. However, graphene is a non-local material that has non-local conductivity and dielectric response, hence it is not clear whether a local model such as the Kubo formula can capture the non-local behavior of graphene. In this thesis, a non-local model called the Lindhard formula is used to calculate graphene's conductivity, and the radiative conductance between two graphene sheets. The Lindhard predictions are compared with the results obtained from the Kubo formula. It is found that at low chemical potential both methods agree, while by increasing the chemical potential of graphene, the Kubo formula overestimates the radiative conductance between two graphene sheets by several orders of magnitude. Increasing the gap size and reducing temperature would increase the difference. It is concluded that the observed differences are due to the simplification involved when deriving the Kubo formula, and therefore it is recommended to use the Lindhard formula in NFRHT studies.

ACKNOWLEDGEMENTS

I would like to thank my advisor, Dr. Sheila Edalatpour for her support, feedback and guidance for the past two years. Also, I would like to acknowledge Dr. Zhihe Jin and Dr. Masoud Rais-Rohani for their help during my career with valuable coursework, technical knowledge and guidance.

I would like to thank my family and friends for their support and encouragement that helped me a lot. Finally, I gratefully acknowledge the Department of Mechanical Engineering and my advisor for the financial support for this research work.

TABLE OF CONTENTS

LIST OF TABLES

LIST OF FIGURES

CHAPTER 1
INTRODUCTION

1.1 Background

Every material with a temperature above zero Kelvin or absolute zero emits electromagnetic waves with a maximum intensity at wavelength of λ_{max}. According to Wien's law [1], λ_{max} is equal to 10 microns at room temperature. The emission of these electromagnetic waves can transfer energy from an object to another, and this process is called the radiative heat transfer (RHT) [2]. The RHT is divided into two distinct regimes called the near-field and far-field regimes. If the distance between the heat exchanging media is more than the dominant wavelength λ_{max}, the heat transfer regime is called the far-field regime. The far-field regime is described by Planck's theory [3] and RHT in this regime is limited to that for blackbodies. As proposed in Max Planck's theory of RHT, the blackbody limit is a great tool for quantifying the rate of RHT because it represents the maximum possible RHT between objects in the far-field. In a far-field regime, only propagating modes contribute to RHT (refer to Fig.1.1). Far-field radiative heat transfer (FFRHT) is modeled using the radiative transfer equation and geometric optic.

The other regime of RHT is called the near-field radiative heat transfer (NFRHT). In this regime, the distance between the objects is less than the dominant wavelength (refer to Fig.1.1). At such small gaps, the contribution of frustrated evanescent modes and surface evanescent modes becomes the dominant RHT method [4, 5, 6, 7, 8]. As shown in Fig.1.1, frustrated evanescent modes are propagative in the emitting medium but they are evanescent in the free space. Surface evanescent modes such as surface phonon polaritons (SPhP) [9, 10] and surface plasmon polaritons (SPP) [11, 12] are evanescent in both the

emitting medium and the free space. SPhPs and SPPs result from the strong coupling between EM waves and phonons or plasmons, respectively [13].

NFRHT is described using the theory of fluctuational electrodynamics [14]. In this theory, the thermally agitation of the charged particles within the emitting medium (which is the source of thermal emission) is modeled using the stochastic current density which is added to Maxwell's equations.

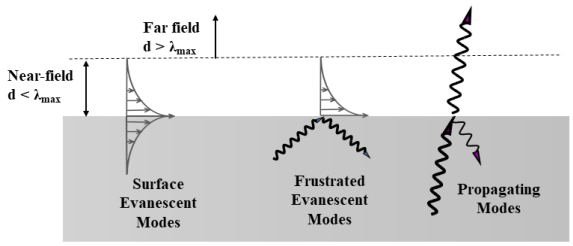

Figure 1.1. FFRHT is dominated by propagating modes while NFRHT includes the contribution of frustrated evanescent modes and surface evanescent modes.

Polder and Van Hove [15] used the formulation in Rytov's work [16] to study the effect of evanescent waves on radiative heat transfer and, upon doing so, paved the way for the emergence of the famous NFRHT. It was theoretically predicted that radiation between closely spaced surfaces could exceed that of blackbody [15, 17, 18, 19, 20], and it was attributed to constructive interference of propagating waves or tunneling of evanescent waves [4]. Evanescent waves can enhance near field radiative heat transfer by several orders of magnitude [4, 5]. The tunneling of evanescent waves decays exponentially with increasing the distance between the heat exchanging media (refer to Fig.1.1); hence their contribution vanishes if the separation gap is larger than the dominant thermal wavelength ($\lambda_{max} = 10\,\mu m$ at room temperature) [21].

The enhanced RHT in near-field has many applications and this concept is being employed in a variety of technologies such as thermal diodes [22, 23], thermophotovoltaics

[24, 25, 26], contactless cooling [27, 28, 29] and thermal rectification [30]. Near-field thermophotovoltaic devices have been experimentally demonstrated recently and are proven to enhance power output by 40-fold compared to the far-field ones [26]. The enhancement of RHT in the near-field regime has also been capitalized on for photonic cooling and solid-state refrigeration [29]. It has also been shown that the surface modes in near-field can achieve a very high thermal rectification ratio of up to 23.7 [30].

Many of these near-field applications rely on spectrally-selective thermal emission that is made possible because of the narrow-band surface polaritons [31]. When most of NFRHT occurs in a very narrow frequency band, RHT is called monochromatic. If the medium supports SPPs or SPhPs, then the NFRHT can be quasi-monochromatic [31, 32, 33].

Polaritonc materials that support SPhPs and SPPs in the near to mid-infrared region are of utmost value since these modes can be thermally excited [26, 29, 30, 31]. The limited number if materials that support SPhPs and SPPs in the near to mid-infrared is the main limitation in taking advantage of the surface evanescent modes in the NFRHT applications. To overcome such deficiency, various metamaterials [34, 35, 36, 37] have been proposed. However, utilizing metamaterials for tuning the spectrum of NFRHT involves significant computational and fabrication costs for design and nanofabrication of these man-made materials.

One of the few materials supporting SPPs in the near and mid-infrared region is graphene [38, 39, 40]. Graphene is an one-atom-thick and two-dimensional allotrope of carbon arranged in a honeycomb lattice. It was discovered in 2004 [41] and has been studied extensively for potential applications in optics, plasmonics, and energy conversion due to its unique thermal, and optical properties [42, 43, 44, 45, 46, 47]. Graphene has proven to be a revolutionary material with massless charge carriers [48, 49] that equips it with surface plasmons in the near and mid-infrared region that can be actively tuned using electric gate voltage and chemical doping [41, 42, 50]. Due to supporting SPPs, graphene

NFRHT can be quasi-monochromatic. Optical and thermal radiation properties of graphene are determined from its electrical conductivity. Two well-known formulas for predicting the electrical conductivity of graphene are Kubo formula and Lindhard formula.

The Kubo formula for graphene's conductivity is a local model that is a function of chemical potential, temperature and frequency [51, 52, 53, 54, 55, 56, 57, 58, 59]. The Kubo model neglects the wavevector dependency of graphene's electrical conductivity.

Another model for calculating the electrical conductivity of graphene is the Lindhard formula which is determined using the framework of Random Phase Approximation (RPA) formula [48, 60, 61, 62]. This model is not only a function of chemical potential, frequency, and temperature, but also considers the wavevector dependency of electrical conductivity and hence provides a great tool to quantify the nonlocal effect of graphene's electrical conductivity. It is worth saying that the Kubo formula is often referred to as the local-RPA as well.

In the next section, a literature review on graphene in the context of NFRHT is provided.

1.2 Literature Review

1.2.1 Theoretical studies

The highly tunable surface plasmons in graphene has a variety of applications in NFRHT. Due to the thinness of graphene sheet, it can be easily placed on dissimilar dielectric materials to enhance their RHT. The surface plasmons in graphene can not only enhance RHT but also can suppress it. This RHT modulation is evident in the work of Joulain et al.[6], and Ilic et al.[56] who reported that a mismatch between SPP frequencies in two media can result in reduced RHT between the two media. For this reason, graphene

has been extensively proposed for modulating NFRHT. Based on modulation characteristics of graphene SPPs, it has been proposed as thermal switch [58, 59, 63, 64, 65, 66] and fast non-contact cooling devices [67]. The versatility of graphene application in NFRHT has been evaluated by calculating the NFRHT between graphene and different material with different dielectric constant such as MoS_2, SiO_2, anisotropic magneto-dielectric hyperbolic metamaterials (AMDHM), black phosphorene and amorphous SiO_2 [68, 69, 70, 71, 72, 73, 74].

Graphene supports SPPs in the infrared region. An SPP resonance frequency in the infrared is of high interest for nano-gap thermophotovoltaic devices, as these frequencies can be thermally excited [46, 53, 75]. Numerical investigation of this phenomenon has shown that applying graphene sheet on a nano-gap TPV cell can enhance energy output significantly [46, 53, 75].

The electrical conductivity of graphene can be tuned in these ways: By changing the chemical potential of graphene that is done by applying gate voltage or chemical doping [35, 76, 77], by applying magnetic field [78] and by applying stress to graphene sheets [79].

Graphene was also studied as a component of metamaterials. One of the drawbacks of metamaterials for NFRHT application is their lack of tunability. Using graphene in metamaterial has been proposed in recent studies and it is shown that the coupling of graphene plasmons with surface modes of other metamaterial components can serve as a mechanism for active tuning of radiative properties of metamaterials [80, 81, 82, 83, 84, 85]. The same mechanism of tuning exists for graphene covered gratings [86].

Graphene/vacuum multi-layers have also been studied in the context of NFRHT, and it has been reported that they demonstrate different characteristic than graphene sheets and metamaterials that include graphene [87, 88]. Increasing the number of sheets can not only blueshift the peak frequency of NFRHT, but it also can increase it as well. Another

observation is that increasing the distance between the sheets can smoothen the temperature gradient between them. This change of temperature gradient can be explained by ultrafast heat transfer between graphene sheets in the near-field regime.

1.2.2 Experimental studies

So far, there are only four experimental studies on NFRHT between graphene sheets or graphene-covered substrates. Experimental work in graphene has proven the findings of existing theoretical investigation. Zwol et al. [89] experimentally demonstrated that when surface plasmons are thermally excited in a system comprising of doped silicon and graphene on SiC, NFRHT is increased by almost 25% at distance smaller than 200 nm.

Another experimental work successfully observes the super-Planck heat transfer in the presence of graphene. The graphene sheets were deposited on silicon substrates in TPV cells and proven to enhance the efficiency of the TPV cell by almost two orders of magnitude at temperature differences above 300 [90].

Recently, another experimental investigation [91] has studied the feasibility of a thermal switch using graphene by applying gate voltage as a mechanism for changing the chemical potential. They separated optical flat coated with graphene and a graphene-coated silicon wafer by 560 nm and imposed two 0 and 35 V gate voltages and shown that the heat flux when bias is imposed is modulated by about 3 to 5%. Another aspect of the proposed device, is that this device is operable in a wide range of temperatures and no moving element exists in that structure. Applying higher gate voltage can also change the behavior of the proposed system. The change of reflectance, transmittance and electrical conductivity of graphene in a wide range of gate voltage is experimentally studied by Li et al. [92]. They observed as gate voltage is increased, the amplitude of change in the electrical conductivity of graphene also increases.

Finally, it is worth noting that due to the Lindhard formula's complexity, most researchers opt for a simplified model called Kubo formula
[51, 52, 53, 54, 55, 56, 57, 58, 59, 60].

1.3 Approach and Contributions

As it is discussed in Section 1.2, graphene is a very promissing materials for applications such as heat transfer enhancement, active control and modulation of heat transfer, thermal switches, nano-gap thermophotovoltaic devices, as well as ultra fast cooling. However, many of these application are being proposed theoretically using a local formula for electrical conductivity of graphene (i.e., the Kubo formula). It is not clear how non-local electrical conductivity of graphene can modify its NFRHT magnitude and SPP resonance frequency. To answer this question, we model near-field radiative conductance of two graphene sheets separated by a vacuum gap using the Kubo formula as well as the Lindhard formula, which is a non-local model. we compared the radiative conductance of graphene sheets obtained using the two formula to understand the non-local effects on NFRHT between graphene sheets.

The results of this study, provides insight into the differences between the two local and non-local modeling approaches. The differences observed between the Kubo and Lindhard formulas results suggest that the non-local effects on NFRHT are significant in most cases.

1.4 Thesis Outline

This thesis is organized as follows. The theoretical background on graphene conductivity formulas is provided in chapter 2. The radiative conductance and dispersion relation expressions are also discussed in this chapter. The research method and the results

of the present study are presented in chapter 3. Conclusion and recommendations are discussed in the fourth chapter.

CHAPTER 2
THEORETICAL BACKGROUND

In this chapter, the fluctuational electrodynamics framework, which is used for modeling near-field radiative heat transfer is discussed. the NFRHT between two graphene covered media is then formulated by applying the fluctuating electrodynamics theory. Next, the surface plasmon polariton modes and their existence in graphene have been discussed.

we discuss how the thermal fluctuations are incorporated into Maxwell's equations. The thermal radiation is then formulated by applying the fluctuating electrodynamics theory, and the NFRHT equations are achieved. The geometry under study is then introduced, and the constituents of the NFRHT equation for the problem under consideration, Fresnel coefficients, are set forth.

2.1 Fluctuational Electrodynamics for Describing Thermal Radiation

Energy flux due to thermal emission of electromagnetic wave, can be found using Poynting vector. The average of Poynting vector over time is expressed as [93]:

$$\langle \mathbf{S}(\mathbf{r},\omega)\rangle = 4 \times \frac{1}{2}\,\mathrm{Re}\,\{\mathbf{E}\times\mathbf{H}^{*}\} \tag{2.1}$$

The **E** and **H** in Eq. 2.1 are the thermally emitted electric and the magnetic fields, respectively. Superscript * denotes complex conjugate and ω is the frequency in rad/s. The factor 4 is included in Eq. 2.1 to account for the fact that only the positive frequencies are considered in the Fourier decomposition of the electromagnetic fields [94, 95]. **E** and **H** are obtained from Maxwell's equations when augmented by the source of thermal emission [93].

The source of thermal emission is the random motion of charge particles in the matter caused by thermal agitation. From a macroscopic paint of view, this random motion can be

modelled using an stochastic current density, $\mathbf{J}^r$, which is added to Maxwell equations. The resulting Maxwell's equations are referred to as the stochastic Maxwell's equations, This framework for modelling thermal radiation is called fluctuational electrodynamics.

$$\begin{aligned}
&\nabla \times \mathbf{E}(\mathbf{r},\omega) = i\omega\mu_0 \mathbf{H}(\mathbf{r},\omega) && \text{(Faraday's law)} \\
&\nabla \times \mathbf{H}(\mathbf{r},\omega) = -i\omega\varepsilon \mathbf{E}(\mathbf{r},\omega) + \mathbf{J}^r(\mathbf{r},\omega) && \text{(Ampere's law)} \\
&\nabla \cdot \mathbf{E}(\mathbf{r},\omega) = 0 && \text{(Gauss's law)} \\
&\nabla \cdot \mathbf{H}(\mathbf{r},\omega) = 0 && \text{(Gauss's law)}
\end{aligned} \tag{2.2}$$

where $\mu_0 = 1.257 \times 10^{-6}$ H/m is the permeability of vacuum, ε is the complex permittivity of the materials, $\mathbf{r}$ is the position vectors, and $\mathbf{J}^r$ is the stochastic current density due to thermally fluctuation of charged particles. The thermally emitted electric and magnetic fields can be written in terms of dyadic Green's function and the fluctuating current as:

$$\begin{aligned}
\mathbf{E}(\mathbf{r},\omega) &= i\omega\mu_0 \textstyle\int_V dV' \overline{\overline{\mathbf{G}}}^E (\mathbf{r},\mathbf{r}',\omega) \cdot \mathbf{J}^r(\mathbf{r}',\omega) = i\omega\mu_0 \int_V dV' G^E_{in} J^r_n \\
\mathbf{H}(\mathbf{r},\omega) &= \textstyle\int_V dV' \overline{\overline{\mathbf{G}}}^H (\mathbf{r},\mathbf{r}',\omega) \cdot \mathbf{J}^r(\mathbf{r}',\omega) = i\omega\mu_0 \int_V dV' G^H_{in} J^r_n
\end{aligned} \tag{2.3}$$

In Eq. 2.3, $\overline{\overline{\mathbf{G}}}^E (\mathbf{r},\mathbf{r}',\omega)$ and $\overline{\overline{\mathbf{G}}}^H (\mathbf{r},\mathbf{r}',\omega)$ are the DGF for electric and magnetic field, respectively and n is the state polarization of the fields observed at $\mathbf{r}$. The DGF can be viewed as a transfer function relating the electric field at point $\mathbf{r}$ to the fluctuating current at point $\mathbf{r}'$ (refer to Fig. 2.1). The electric and magnetic DGFs are obtained by solving the Maxwell equations for a point source located at location $\mathbf{r}'$.

Using the relations established between the stochastic current density and the magnetic and electric fields, the energy flux can be obtained by inserting Eq. 2.3 into Eq. 2.1, as:

$$\begin{aligned}
&\langle \mathbf{S}(\mathbf{r},\omega) \rangle \\
&= 4 \times \tfrac{1}{2} \operatorname{Re} \{ \mathbf{E}(\mathbf{r},\omega) \times \mathbf{H}^*(\mathbf{r},\omega) \} \\
&= 2\omega\mu_0 \operatorname{Re} \left\{ i \textstyle\int_V dV' \int_V dV'' G^E_{n\alpha}(\mathbf{r},\mathbf{r}',\omega) G^{H^*}_{n\beta}(\mathbf{r},\mathbf{r}'',\omega') \left\langle J^r_\alpha(\mathbf{r}',\omega) J^{r^*}_\beta(\mathbf{r}'',\omega') \right\rangle \right\}
\end{aligned} \tag{2.4}$$

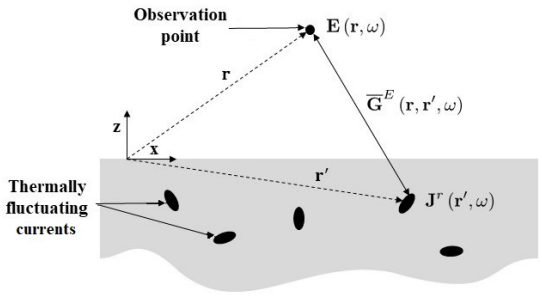

Figure 2.1. DGF can be viewed as a transfer function relating the thermally fluctuating current at location **r**' to the electric field at location **r**.

Since the thermal fluctuations of charged particles cause the stochastic current density $\mathbf{J}^r$, the ensemble average of the correlation function of the fluctuating current, i.e., the term $\left\langle J_\alpha^r(\mathbf{r}',\omega)\, J_\beta^{r^*}(\mathbf{r}'',\omega')\right\rangle$, that is the source of thermal radiation should be related to the temperature of the emitter. This relation is established by the fluctuation-dissipation theorem [96]. Under the same assumptions as of the Maxwell equations and assuming that the material is in thermal equilibrium, the ensemble average of the correlation function of the fluctuating current is given by:

$$\left\langle J_\alpha^r(\mathbf{r}',\omega)\, J_\beta^{r^*}(\mathbf{r}'',\omega')\right\rangle = \frac{\omega\varepsilon_0\varepsilon''}{\pi}\Theta(\omega,T)\delta(\mathbf{r}'-\mathbf{r}'')\delta(\omega-\omega') \tag{2.5}$$

where $\Theta(\omega,T)=\hbar\omega/\left(\exp\left(\hbar\omega/k_BT\right)-1\right)$ is the mean energy of a Planck oscillator [82, 84, 97], ε'' is the imaginary part of the dielectric function of the material, $\varepsilon_0 = 8.854\times10^{-12}$ F/m is the permittivity of the vacuum, $\hbar = h/2\pi = 1.0546\times10^{-3}J.s$ is the reduced Planck constant and $k_B = 1.381\times10^{-23}J/K$ is the Boltzmann constant. Therefore, by applying the fluctuation-dissipation theorem to Eq. 2.4 and using ergodic hypothesis, the radiative heat flux is found as:

$$\begin{aligned}&\langle\mathbf{S}(\mathbf{r},\omega)\rangle = \\ &\tfrac{2k_0^2\Theta(\omega,T)}{\pi}\,\mathrm{Re}\left\{i\varepsilon_r''(\omega)\int_V dV' G_{n\beta}^{E}(\mathbf{r},\mathbf{r}',\omega)\, G_{n\alpha}^{H^*}(\mathbf{r},\mathbf{r}'',\omega')\right\}\end{aligned} \tag{2.6}$$

In Eq. 2.6, $k_0 = \omega/c_0$ is the wavevector in the vacuum, where $c_0 = \sqrt{\varepsilon_0 \mu_0}$ is the speed of light in vacuum.

2.2 Near-Field Radiative Heat Transfer Between Two Graphene Covered Semi-Infinite Media

In this section, NFRHT between two graphene-covered planar bodies is derived. The schematic of the problem under consideration is shown in Fig. 2.2 where two semi-infinite media are covered with graphene sheets. It is realistically assumed that graphene sheets' temperature is equal to the medium's temperature on which they are placed. The emitter and the receiver are kept at the constant temperatures of T_1 and T_3, respectively, and a vacuum gap of length D separates the two media.

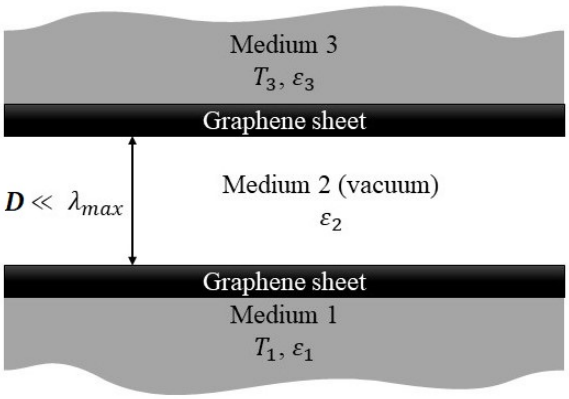

Figure 2.2. Schematic of the problem under consideration. Two graphene-covered media (media 1 and 3), with permittivities ε_1 and ε_3 are kept at temperatures T_1 and T_3, respectively, and they are separated by a vacuum gap (medium 2) of size D, $\varepsilon_2 = 1$.

The NFRHT flux from medium 1 to medium 3 is calculated using Eq. 2.6 in which the only unknowns are Green's functions $G_{13}^{E}(\mathbf{r}, \mathbf{r}', \omega)$ and $G_{13}^{H}(\mathbf{r}, \mathbf{r}', \omega)$. For the

one-dimensional geometry shown in Fig. 2.2, the DGFs in the free space (Eq. 2.3) are the solution of the following equation [97]:

$$\nabla \times \nabla \times \overline{\overline{\mathbf{G}}}^{E}(\mathbf{r}, \mathbf{r}', \omega) - k^2 \overline{\overline{\mathbf{G}}}^{E}(\mathbf{r}, \mathbf{r}', \omega) = \overline{\overline{\mathbf{I}}} \delta(\mathbf{r} - \mathbf{r}') \tag{2.7}$$

In Eq. 2.7, $\overline{\overline{\mathbf{I}}}$ is the identity matrix. The solution for the magnetic DGF can be obtained using the solution of the electric DGF as $\overline{\overline{\mathbf{G}}}^{H}(\mathbf{r}, \mathbf{r}', \omega) = \nabla \times \overline{\overline{\mathbf{G}}}^{E}(\mathbf{r}, \mathbf{r}', \omega)$. Since the geometry under consideration has azimuthal symmetry, the polar coordinate will be utilized instead of the Cartesian coordinate. The solution of Eq. 2.7 is provided in Ref. [98]. After using this solution for $G_{13}^{E}(\mathbf{r}, \mathbf{r}', \omega)$ and $G_{13}^{H}(\mathbf{r}, \mathbf{r}', \omega)$, the integral term in Eq. 2.6 can be written as [99]:

$$\begin{aligned} &\textstyle\int_{V_1} dV' G_{13i\alpha}^{E}(\mathbf{r}, \mathbf{r}', \omega) G_{13j\alpha}^{H^*}(\mathbf{r}, \mathbf{r}', \omega) = \\ &\textstyle\int_{-\infty}^{\infty} \frac{d\mathbf{k}_\rho}{(2\pi)^2} \int_z dz' g_{13i\alpha}^{E}(k_\rho, z, z', \omega) g_{13j\alpha}^{H^*}(k_\rho, z, z', \omega) \end{aligned} \tag{2.8}$$

where $g_{13i\alpha}^{E}$ and $g_{13j\alpha}^{H}$ are the Weyl components of DGF [98, 99], k_ρ is the parallel component of the wavevector (refer to Fig. 2.3) and z and z′ are the z components of the location vectors $\mathbf{r}$ and $\mathbf{r}'$ (See Fig. 2.1). The complex wavevectors in medium 1 and 3 are k_1 and k_3, respectively with $k_1^2 = \varepsilon_1 k_0^2$ and $k_3^2 = \varepsilon_3 k_0^2$. The normal component of the wavevector in medium j is calculated as $k_{zj} = \sqrt{k_j^2 - k_\rho^2}$. The parallel component of the wavevector which has components along x and y directions can be written as $\mathbf{k}_\rho = k_x \hat{\mathbf{x}} + k_y \hat{\mathbf{y}}$. By expressing $\mathbf{k}_\rho$ in the polar coordinate system and considering azimuthal symmetry, $\int_{-\infty}^{\infty} d\mathbf{k}_\rho$ can be written as [93]:

$$\int_{-\infty}^{\infty} d\mathbf{k}_\rho = \int_{-\infty}^{\infty} \int_{-\infty}^{\infty} dk_x dk_y = \int_{k_\rho=0}^{\infty} \int_{\phi=0}^{2\pi} k_\rho dk_\rho d\phi = 2\pi \int_{k_\rho=0}^{\infty} k_\rho dk_\rho \tag{2.9}$$

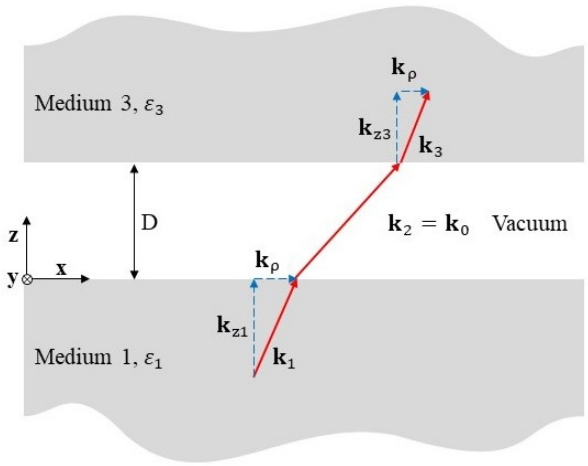

Figure 2.3. The complex wavevector in medium 1 and 3 has a component parallel to the surface of the medium (k_ρ) and a normal component (k_z).

Substituting Eq. 2.8 and 2.9 into Eq. 2.6, the near-field radiative heat flux from medium 1 to medium 3 is equal to [100]:

$$q''_{\omega,13} = \frac{k_0^2 \Theta(\omega,T_1)}{\pi^2} \times \mathrm{Re}\left\{ i\varepsilon_1'' \int_{k_\rho=0}^{\infty} k_\rho dk_\rho \int_z dz' \begin{bmatrix} g^E_{13\rho\alpha}\left(k_\rho,z,z',\omega\right) g^{H^*}_{13\theta\alpha}\left(k_\rho,z,z',\omega\right) \\ -g^E_{13\theta\alpha}\left(k_\rho,z,z',\omega\right) g^{H^*}_{13\rho\alpha}\left(k_\rho,z,z',\omega\right) \end{bmatrix} \right\} \tag{2.10}$$

The integral over k_ρ from 0 to ∞ (i.e., $\int_{k_\rho=0}^{\infty}$) in Eq. 2.10 can be divided into two parts: an integral from 0 to k_0 ($\int_{k_\rho=0}^{k_0}$) and an integral from k_0 to ∞ ($\int_{k_\rho=k_0}^{\infty}$). The first integral is over EM wares with $k_\rho < k_0$. Therefore, these wave are propagative in the Vacuum gap. The flux of heat transferred by these propagating wares is referred to as $q''^{\mathrm{prop}}_{\omega}$ in this thesis. The second integral is over waves with $k_\rho > k_0$. Hence, these waves are evanescent in separation gap.

These modes, which evanescently decay perpendicular to the surface in a distance approximately equal to the dominant wavelength of thermal radiation λ, can contribute to heat transfer if the separation gap is less than λ (i.e., when $D \leqslant \lambda$). The flux of heat transfer from medium 1 to medium 3 due to the evanescent waves is shown by $q''^{\mathrm{evan}}_{\omega}$ in this

thesis [101, 102, 99]. Hence the spectral flux of NFRHT from medium 1 to medium 3 can be written as:

$$q''_{\omega,13} = q''^{\text{prop}}_{\omega,13} + q''^{\text{evan}}_{\omega,13} \tag{2.11}$$

When the appropriate form of Weyl components of DGF [98, 99, 103] are substituted into Eq. 2.10, $q''_{\omega,13}$ can be written as:

$$\begin{aligned} q''^{\text{prop}}_{\omega,13} &= \tfrac{\Theta(\omega,T_1)}{4\pi^2} \int_0^{k_0} \textstyle\sum_{\gamma=\text{TE,TM}} k_\rho Z^{\text{prop}}_{13} dk_\rho \\ q''^{\text{evan}}_{\omega,13} &= \tfrac{\Theta(\omega,T_1)}{\pi^2} \int_{k_0}^{\infty} \textstyle\sum_{\gamma=\text{TE,TM}} k_\rho Z^{\text{evan}}_{13} dk_\rho \end{aligned} \tag{2.12}$$

where

$$\begin{aligned} Z^{\text{prop}}_{13} &= \frac{\left(1-\left|r^\gamma_{21}\right|^2\right)\left(1-\left|r^\gamma_{23}\right|^2\right)}{\left|1-r^\gamma_{21}r^\gamma_{23}e^{2ik'_{22}2d}\right|^2} \\ Z^{\text{evan}}_{13} &= \frac{\text{Im}\left(r^\gamma_{21}\right)\text{Im}\left(r^\gamma_{23}\right)}{\left|1-r^\gamma_{21}r^\gamma_{23}e^{-2k''_{z2}d}\right|^2} \end{aligned} \tag{2.13}$$

The heat flux transferred from medium 3 to medium 1 ($q''_{\omega,31}$) can be found similarly as:

$$\begin{aligned} q''^{\text{prop}}_{\omega,31} &= \tfrac{\Theta(\omega,T_3)}{4\pi^2} \int_0^{k_0} \textstyle\sum_{\gamma=\text{TE,TM}} k_\rho Z^{\text{prop}}_{31} dk_\rho \\ q''^{\text{evan}}_{\omega,31} &= \tfrac{\Theta(\omega,T_3)}{\pi^2} \int_{k_0}^{\infty} \textstyle\sum_{\gamma=\text{TE,TM}} k_\rho Z^{\text{evan}}_{31} dk_\rho \end{aligned} \tag{2.14}$$

The net heat flux from medium 1 to medium 3, q''_ω, can then be obtained as:

$$q''_\omega = q''_{\omega,13} - q''_{\omega,31} \tag{2.15}$$

Substituting $q''_{\omega,13}$ and $q''_{\omega,31}$ from Eqs. 2.12 and 2.14, q''_ω is found as:

$$\begin{aligned} q''^{\text{prop}}_{\omega} &= \tfrac{\Theta(\omega,T_1)-\Theta(\omega,T_3)}{4\pi^2} \int_0^{k_0} \textstyle\sum_{\gamma=\text{TE,TM}} k_\rho Z^{\text{prop}}_{13} dk_\rho \\ q''^{\text{evan}}_{\omega} &= \tfrac{\Theta(\omega,T_1)-\Theta(\omega,T_3)}{\pi^2} \int_{k_0}^{\infty} \textstyle\sum_{\gamma=\text{TE,TM}} k_\rho Z^{\text{evan}}_{13} dk_\rho \end{aligned} \tag{2.16}$$

where Θ is the mean energy of a Planck oscillator, D is the distance between the two media, k''_{z2} is the imaginary part of the z-component of the wavevector in medium 2, γ shows the polarization of waves (TE for the transverse electric and TM for transverse magnetic polarization) and r_{ij} is the Fresnel reflection coefficient at the interface of media i and j (refer to Fig. 2.4). The Fresnel reflection coefficients for the TE and TM polarizations can be expressed as [104, 105]:

$$\begin{aligned} r_{ij}^{TE} &= \frac{k_{zi} - k_{zj} - \mu_0 \sigma\left(\omega, k_\rho, T\right)\omega}{k_{zi} + k_{zj} + \mu_0 \sigma\left(\omega, k_\rho, T\right)\omega} \\ r_{ij}^{TM} &= \frac{\varepsilon_j k_{zi} - \varepsilon_i k_{zj} + \frac{\sigma(\omega, k\rho, T) k_{zi} k_{zj}}{\varepsilon_0 \omega}}{\varepsilon_j k_{zi} + \varepsilon_i k_{zj} + \frac{\sigma(\omega, k_\rho, T) k_{zi} k_{zj}}{\varepsilon_0 \omega}} \end{aligned} \tag{2.17}$$

In Eq. 2.17, ε_i and ε_j are the dielectric functions of media i and j, respectively, and σ is the electrical conductivity of graphene.

Equation 2.16 is obtained by assuming that media 1 and 3 are optically thick. In other words, it is assumed that thermal radiation incident on these media cannot escape the backside of these media as they are thick enough such that they will absorb thermal radiation before it exits from the other end. In the case of suspended graphene sheets (with no substrate), thermal radiation can be transmitted through the graphene. In this case, the Weyl component of the DGFs also include Fresnel transmission coefficient. In this case:

$$\begin{aligned} Z_{13}^{\text{prop}} &= \frac{\left(1 - \left|r_{21}^\gamma\right|^2 - \left|t_{21}^\gamma\right|^2\right)\left(1 - \left|r_{23}^\gamma\right|^2 - \left|t_{23}^\gamma\right|^2\right)}{\left|1 - r_{21}^\gamma r_{23}^\gamma e^{2ik_{z2}D}\right|^2} \\ Z_{13}^{\text{evan}} &= \frac{\text{Im}\left(r_{21}^\gamma\right)\text{Im}\left(r_{23}^\gamma\right)}{\left|1 - r_{21}^\gamma r_{23}^\gamma e^{2ik_{z2}D}\right|^2} \end{aligned} \tag{2.18}$$

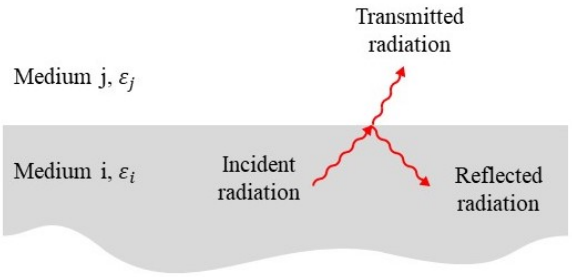

Figure 2.4. The Fresnel reflection (r_{ij}) and transmission coefficients (t_{ij}) describe the reflection or transmission of EM waves incident on the interface between medium i and j.

In Eq. 2.18, t_{ij}^{γ} is the Fresnel transmission coefficient (refer to Fig. 2.4). The transmission coefficient is given by [104, 105]:

$$\begin{aligned} t_{ij}^{\mathrm{TE}} &= \frac{2k_{zi}}{k_{zi}+k_{zj}+\mu_0\sigma\left(k_\rho,\omega,T\right)\omega} \\ t_{ij}^{\mathrm{TM}} &= \sqrt{\frac{\varepsilon_i}{\varepsilon_j}\,\mathrm{Re}\left[\frac{k_{zj}}{k_{zi}}\right]}\,\frac{2\varepsilon_j k_{zi}}{\varepsilon_j k_{zi}+\varepsilon_i k_{zj}+\frac{\sigma(k_\rho,\omega,T)k_{zi}k_{zj}}{\varepsilon_0\omega}} \end{aligned} \tag{2.19}$$

The radiative conductance between media 1 and 3 is defined as :

$$G_\omega = \lim_{\delta T\to 0}\frac{q''_\omega}{\delta T} \tag{2.20}$$

where q''_ω is the heat flux between the two media and δT is their temperature difference. Substituting for q''_ω from Eq. 2.16, the radiative conductance is found as:

$$\begin{aligned} G_\omega^{\mathrm{prop}} &= \tfrac{1}{4\pi^2}\tfrac{\partial\Theta}{\partial T}\int_0^{k_0}\textstyle\sum_{\gamma=\mathrm{TE,TM}} Z_{13}^{\mathrm{prop}}k_\rho dk_\rho \\ G_\omega^{\mathrm{evan}} &= \tfrac{1}{4\pi^2}\tfrac{\partial\Theta}{\partial T}\int_{k_0}^{\infty}\textstyle\sum_{\gamma=\mathrm{TE,TM}} Z_{13}^{\mathrm{evan}}k_\rho dk_\rho \end{aligned} \tag{2.21}$$

In Eq. 2.21, G_ω^{prop} and G_ω^{evan} are the propagating and evanescent part of the radiative conductance.

2.3 Graphene Electrical Conductivity Models

As seen from Eqs. 2.17 and 2.19, the reflection and transmission coefficients and thus radiative heat flux strongly depend on the graphene electrical conductivity. So far, NFRHT in graphene-based media is calculated using the Kubo formula for the electrical conductivity. The Kubo formula is obtained by assuming that $k_\rho = 0$. Since this expression does not account for the variation of σ with k_ρ, it is referred to as a local model. As discussed previously, radiative heat transfer can be mediated by all electromagnetic waves having a k_ρ between 0 and infinity. Therefore, using the Kubo formula for near-field radiative heat transfer calculations can be questionable.

There is another model for electrical conductivity of graphene, referred to as the Lindhard formula [106, 61], which accounts for the variation of σ with k_ρ as well. These two formulas for the electrical conductivity of graphene are discussed in the following subsections.

2.3.1 Kubo Formula

Ignoring the impact of magnetic field, the Kubo formulation is [39, 107, 50, 104, 108]:

$$\begin{aligned}\sigma(\omega, \mu_c, T) = &-\frac{ie^2(\omega+i\gamma)}{\pi\hbar^2}\Big(\frac{1}{(\omega+i\gamma)^2}\int_0^\infty E\left(\frac{\partial f(E)}{\partial E} - \frac{\partial f(-E)}{\partial E}\right)dE \\ &- \int_0^\infty \frac{f(-E)-f(E)}{(\omega+i\gamma)^2-4(E/\hbar)^2}dE\Big)\end{aligned} \tag{2.22}$$

where $f(E) = \{1 + \exp[(E-\mu_c)/k_\mathrm{B}T]\}^{-1}$ is the Fermi distribution function, e is the elementary charge, $\gamma = \tau^{-1}$ is the electron scattering rate, $\tau = \mu_m\mu_c/e\nu_F^2$ is the electron relaxation time in graphene where μ_m is the carrier mobility, $\nu_F = 9.5 \times 10^5 m/s$ is the Fermi velocity, and μ_c is the chemical potential of graphene in Joules (J). The first and second terms in Eq. 2.22 correspond to the intraband and interband electron transitions,

respectively [109]. When the integrations in Eq. 2.22 are performed, the Kubo electrical conductivity can be written as:

$$\sigma = \sigma^{\text{intra}} + \sigma^{\text{inter}} \tag{2.23}$$

In Eq. 2.23, σ^{intra} and σ^{inter} refer to electrical conductivity due to intraband and interband transitions, respectively, and they are given by:

$$\begin{aligned} \sigma^{\text{intra}}(\omega, \mu_c, T) &= \tfrac{\sigma_0}{\pi} \tfrac{4}{\hbar\gamma - i\hbar\omega} \left[\mu_c + 2k_B T \ln\left(1 + e^{-\mu_c/k_B T}\right)\right] \\ \sigma^{\text{inter}}(\omega, \mu_c, T) &= \sigma_0 \left[G(\hbar\omega/2) + i\tfrac{4\hbar\omega}{\pi} \int_0^\infty \tfrac{G(E) - G(\hbar\omega/2)}{(\hbar\omega)^2 - 4E^2} dE\right] \end{aligned} \tag{2.24}$$

where

$$G(x) = \frac{\sinh\left(\frac{x}{k_B T}\right)}{\cosh\left(\frac{\mu_c}{k_B T}\right) + \cosh\left(\frac{x}{k_B T}\right)} \tag{2.25}$$

and $\sigma_0 = e^2/(4\hbar)$. It is shown that the intraband contribution is dominant in the THz and far-infrared regions, while the interband plays a significant role in the near-infrared and visible regions [110]. contribution from both interband ad intraband transitions are accounted for in this study.

2.3.2 Lindhard Formula

The Lindhard formula provides a wavevector-dependent conductivity for graphene as [111]:

$$\sigma(k_\rho, \omega, \mu_c T) = ie^2 \frac{\omega}{k_\rho^2} \chi(k_\rho, \omega, \mu_c, T) \tag{2.26}$$

where $\chi\left(k_\rho, \omega, \mu_c, T\right)$ is the susceptibility of graphene. The susceptibility of graphene is a complex number and is expressed as:

$$\chi\left(k_\rho, \omega, \mu_c, T\right) = \mathrm{Re}\left[\chi\left(k_\rho, \omega, \mu_c, T\right)\right] + i\,\mathrm{Im}\left[\chi\left(k_\rho, \omega, \mu_c, T\right)\right] \tag{2.27}$$

The real and imaginary parts in Eq. 2.27 are given using the Lindhard formula as [61]:

$$\begin{aligned}\mathrm{Re}\left[\chi\left(k_\rho, \omega, \mu_c, T\right)\right] = \frac{1}{\pi}\sum_{\alpha=\pm}\Big(&\frac{-2k_BT\ln\left(1+e^{\alpha\mu_c/k_BT}\right)}{\left(\hbar v_F\right)^2} + H(\hbar\omega - \hbar v_F k_\rho)\\ &\times k_\rho^2 f\left(\hbar\omega, \hbar v_F k_\rho\right)\left[G_-^{(\alpha)}\left(k_\rho, \omega, T\right) - G_+^{(\alpha)}\left(k_\rho, \omega, T\right)\right] + H(\hbar v_F k_\rho - \hbar\omega)\\ &\times k_\rho^2 f\left(\hbar v_F k_\rho, \hbar\omega\right)\left[-\frac{\pi}{2}\delta_{\alpha,-} + D_-^{(\alpha)}\left(k_\rho, \omega, T\right)\right]\Big)\end{aligned} \tag{2.28}$$

$$\begin{aligned}\mathrm{Im}\left[\chi\left(k_\rho, \omega, \mu_c, T\right)\right] = \frac{1}{\pi}\sum_{\alpha=\pm}\Big(&H\left(\hbar v_F k_\rho - \hbar\omega\right)k_\rho^2 f\left(\hbar v_F k_\rho, \hbar\omega\right)\\ &\times\left[G_+^{(\alpha)}\left(k_\rho, \omega, \mu_c, T\right) - G_-^{(\alpha)}\left(k_\rho, \omega, T\right)\right] + H\left(\hbar\omega - \hbar v_F k_\rho\right)k_\rho^2 f\left(\hbar\omega, \hbar v_F k_\rho\right)\\ &\times\left[-\frac{\pi}{2}\delta_{\alpha,-} + D_+^{(\alpha)}\left(k_\rho, \omega, T\right)\right]\Big)\end{aligned} \tag{2.29}$$

In Eqs. 2.28 and 2.29, H(x) is the Heaviside step function, and,

$$\begin{aligned} &f(x,y) = \tfrac{1}{2\sqrt{x^2-y^2}}\\ &G_\pm^{(\alpha)}\left(k_\rho, \omega, \mu_c, T\right) = \int_1^\infty \frac{\sqrt{u^2-1}}{\exp\left(\frac{\left|\hbar v_F k_\rho u \pm \hbar\omega\right| - 2\alpha\mu_c}{2k_BT}\right)+1}du\\ &D_\pm^{(\alpha)}\left(k_\rho, \omega, \mu_c, T\right) = \int_{-1}^1 \frac{\sqrt{1-u^2}}{\exp\left(\frac{\left|\hbar v_F k_\rho u \pm \hbar\omega\right| - 2\alpha\mu_c}{2k_BT}\right)+1}du\end{aligned} \tag{2.30}$$

The electrical conductivity calculated using Eq. 2.26 through 2.30 is referred to as the Lindhard formula for graphene's electrical conductivity. The Lindhard formula has not been used in NFRHT calculations. Hence, the effect of wavevector dependency on NFRHT problems involving graphene has not been investigated yet.

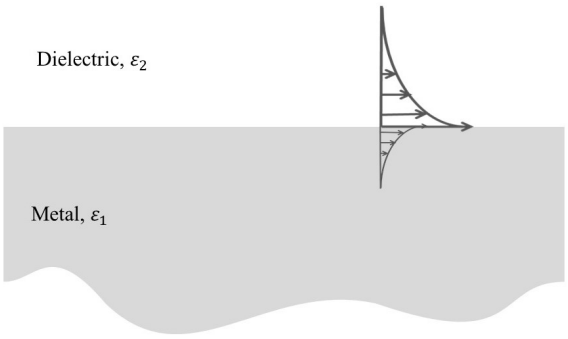

Figure 2.5. The SPPs appear in the interface of metal and dielectric with permittivities of ε_1 and ε_2, respectively and decay exponentially away from the surface.

2.4 Surface Plasmon Polaritons

When the real part of the dielectric function changes sign at the interface of two materials, the coherent oscillations of delocalized electrons result in thermal emission of a type of surface modes called surface plasmon polaritons. The existence of these modes, which usually have a significant amount of energy, causes a peak in NFRHT. The existence of this peak is highly demanded for NFRHT applications such as nano-gap thermophotovoltaic devices.

The field generated by surface plasmons is confined near the surface and its amplitude decays exponentially by moving away from the interface [9, 112, 113, 114] (refer to Fig. 2.5). SPPs are non-propagating surface waves because the wavevector is larger than the vacuum wavevector. These surface waves also do not couple to propagating electromagnetic waves in a vacuum [115]. The magnitude of the wavevector of the SPPs excited at a metal-dielectric interface (semi-infinite metallic and dielectric media) is expressed as:

$$|k_{sp}| = k_0 \sqrt{\frac{\varepsilon_1 \varepsilon_2}{\varepsilon_1 + \varepsilon_2}} \tag{2.31}$$

where ε_1 and ε_2 are the dielectric functions of the metallic and dielectric media (refer to Fig. 2.5).

SPPs in metals are not tunable and have high energy loss [116, 117]. They also get excited in the visible range. Thermal excitation of metal SPPs requires high temperatures, which limits their application in NFRHT [118]. The search for a material with better SPP characteristics has unveiled graphene as a potential candidate.

2.5 Graphene Surface Plasmons

In this section, the dispersion relation of graphene plasmons, which relate the wavevector and the frequency of these modes, is derived.

As mentioned before, the frequency of graphene SPPs, unlike metal SPPs, can be tuned by controlling graphene's charge densities via electrical gating or chemical doping [107, 119, 120, 121]. Graphene SPPs get excited in near-infrared to terahertz regions [121, 122] depending on the chemical potential of graphene which is highly demanded for NFRHT applications.

Here, we consider the structure shown in Fig. 2.6, where two graphene covered dielectric media with permittivity ε_1 and ε_2 are separated by a vacuum gap of size D. We derive the dispersion relation for the bottom graphene sheet. The electric and magnetic fields propagate along the z-direction. Graphene supports both TE and TM modes, but TE SPPs in graphene are not appropriately confined, and hence are not of interest for high-confinement applications such as NFRHT [123].

For TM-polarized SPPs with the parallel wavevector of k_ρ, the magnetic field can be written as:

$$\begin{aligned} H_y &= Ae^{-\kappa_3 x}e^{ik_\rho z} \qquad x > 0 \\ H_y &= Be^{\kappa_1 x}e^{ik_\rho z} \qquad x < 0 \end{aligned} \tag{2.32}$$

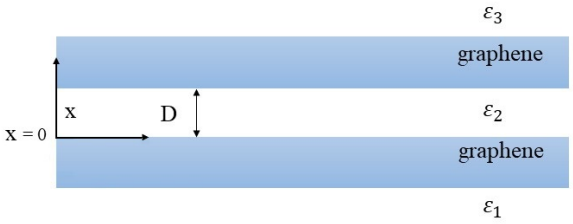

Figure 2.6. The graphene sheet structure which can support SPP modes sandwiched between two surrounding media.

where A and B are undetermined coefficients and $\kappa_j = \sqrt{k_\rho^2 - \varepsilon_j k_0^2}$. The electric field component in the z direction for $0 < x < D$ can be found from Maxwell's equations as:

$$E_z = -i\frac{1}{\omega\varepsilon_0\varepsilon_2}\frac{\partial H_y}{\partial x} \tag{2.33}$$

The boundary conditions at $x = 0$ and $x = D$ are:

$$\begin{aligned} &\mathrm{E_{x1}}(0) = \mathrm{E}_{x2}(0) \quad \text{and} \quad H_{y1}(0) - H_{y2}(0) = \sigma_1 E_{x1}(0) \quad \text{at } z = 0 \\ &\mathrm{E}_{x2}(d) = \mathrm{E}_{x3}(d) \quad \text{and} \quad H_{y2}(d) - H_{y3}(d) = \sigma_2 E_{x2}(d) \quad \text{at } z = d \end{aligned} \tag{2.34}$$

where the numeric subscripts show the region of interest (refer to Fig. 2.6). By solving Eqs. 2.32 and 2.33 and imposing the boundary conditions in Eq. 2.34, the following expressions for the dispersion relation of graphene's SPPs can be obtained.

$$\begin{aligned} &\tfrac{\varepsilon_2}{\kappa_2}\tanh\left(\kappa_2 D/2\right) + \tfrac{\varepsilon_1}{\kappa_1} + i\tfrac{\sigma}{\omega\varepsilon_0} = 0 \\ &\tfrac{\varepsilon_2}{\kappa_2}\coth\left(\kappa_2 D/2\right) + \tfrac{\varepsilon_1}{\kappa_1} + i\tfrac{\sigma}{\omega\varepsilon_0} = 0 \end{aligned} \tag{2.35}$$

CHAPTER 3
RESEARCH METHOD AND RESULTS

In this chapter, we discuss the implementation of the Kubo and Lindhard models for electrical conductivity of graphene in MATLAB in Section 3.1. In Section 3.2 the Kubo, Lindhard, and the NFRHT codes are verified against data available in literature. Finally, in Section 3.3 a thorough comparison of the radiative conductance between two graphene sheets as obtained using the Kubo and Lindhard models is conducted. Since the the Lindhard model captures the wavevector-dependence of the electrical conductivity of graphene, the effect of the temperature and gap size on the radiative conductance of the problem under consideration is studied using this model. Copies of the developed codes are provided in the appendix.

3.1 Research Method

In this thesis, the Kubo (Eq. 2.22) and Lindhard (Eqs. 2.28 and 2.29) models for electrical conductivity of graphene, the model for near-field radiative conductance between graphene sheets (Eq, 2.21), as well as the dispersion relation of graphene (Eq. 2.35) are implemented in MATLAB. A diagram for the developed code structures is shown in Fig. 3.1 and 3.2.

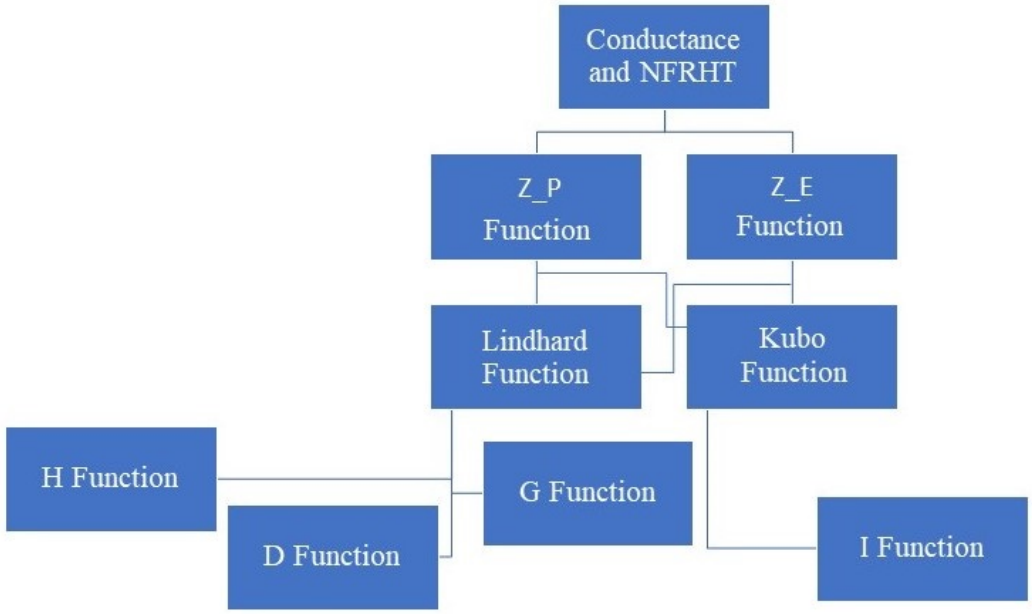

Figure 3.1. The structure of the codes developed for calculation of NFRHT and near-field radiative conductance.

The radiative conductance (G) and the NFRHT are implemented using the code structure in Fig. 3.1 (refer to Eq. 2.16 and 2.21). Z_P and Z_E are the propagating and evanescent exchange functions shown in Eq. 2.18. The calculation of the Fresnel reflection and transmission coefficients requires the calculation of the electrical conductivity of graphene (refer to Eqs. 2.17 and 2.19). Hence the Z_P and Z_E functions call the Kubo and Lindhard functions in which graphene's electrical conductivity is implemented. The Kubo formula (Eq. 2.24) has an integral part, and the integral in σ^{inter} is calculated using the I function in the code. On the other hand, the Lindhard formula (refer to Eqs. 2.28 and 2.29) involves H, G, and D functions (refer to Eq. 2.30) that are implemented in functions with the same name (Fig. 3.1).

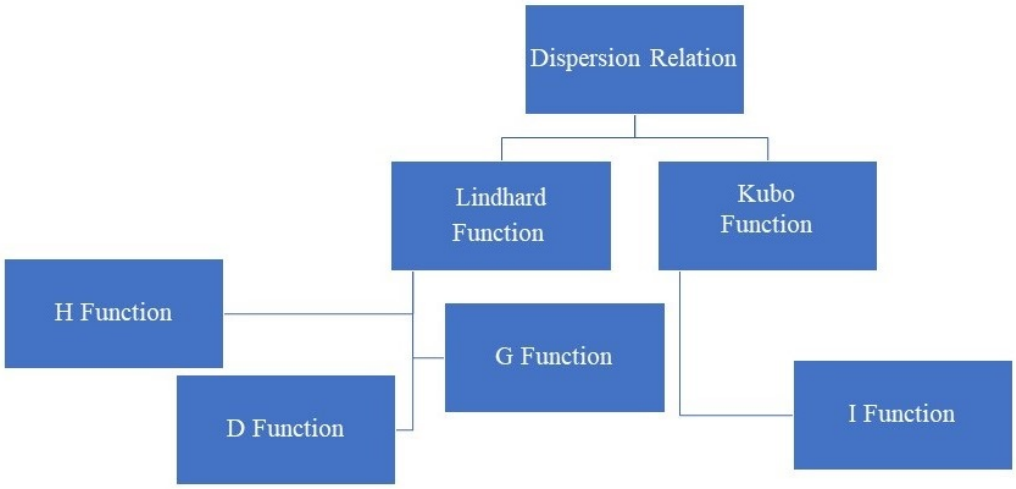

Figure 3.2. The structure of the codes developed for calculation of the dispersion relation.

The structure of the codes developed for the dispersion relation is a function of the graphene's electrical conductivity, wavevector, gap size, frequency, and the permittivity of the surrounding media (refer to Eq. 2.35). Therefore, the only functions needed for dispersion relation are the Kubo and the Lindhard functions. To solve Eq. 2.35, which is as implicit function, an optimization technique of MATLAB named *fminbnd* is used. *fminbnd* is a one-dimensional minimization technique that minimizes the function in a specified range. The functions are minimized with respect to the parallel component of wavevector.

3.2 Verification

In this section, the developed codes for calculating the Kubo and Lindhard formulas for the electrical conductivity of graphene as well as the code developed for NFRHT are verified against the data available in the literature.

3.2.1 Kubo Formula

For verification of the developed Kubo code, a graphene sheet was assumed at $T = 300K$, $\mu_c = 0.3eV$ and scattering rate $(\gamma) = 5.62 \times 10^{12} s^{-1}$. The electrical conductivity of graphene has been computed using the developed MATLAB code for the Kubo formula (refer to appendix A). The result of the MATLAB code for the electrical conductivity using the Kubo formula is compared with the electrical conductivity of graphene reported in Ref. [124] for the same T and μ_c in Fig. 3.3. The conductivity is normalized by σ_0 (refer to Eq. 2.24). As it is seen from Fig. 3.3, the result of the Kubo code in the present study is in great agreement with the data in Ref. [124].

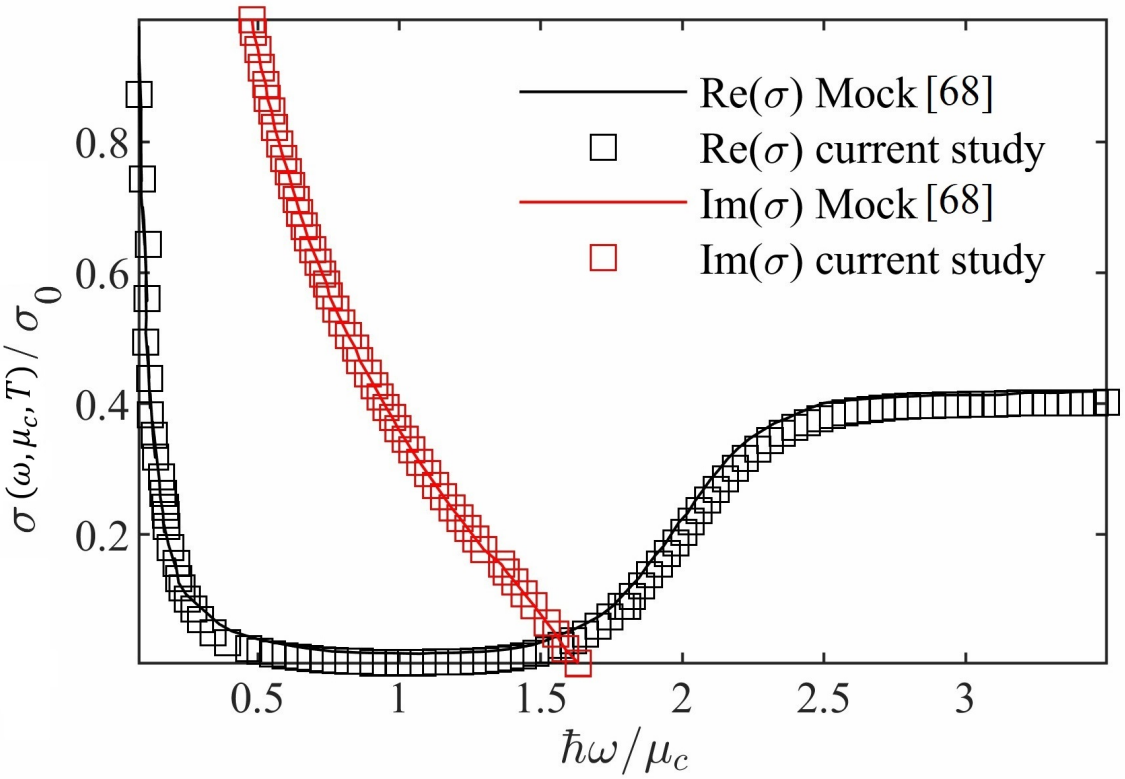

Figure 3.3. Verification of the Kubo code against the data available in Ref. [68] for $\mu_c = 0.3$ eV, $T = 300$ K and $\gamma = 5.62 \times 10^{12} s^{-1}$.

3.2.2 Lindhard Formula

For verification of the developed Lindhard code, a free-standing graphene sheet at $T = 0$ K and $\omega = 0$ rad/s was considered. Graphene's susceptibility is computed using the developed MATLAB code for the Lindhard formula (refer to appendix A), which can then be converted to electrical conductivity by Eq. 2.26.

The result of the MATLAB code for the susceptibility using the Lindhard formula is compared with the susceptibility of graphene reported in Ref. [61] for the same T and ω in Fig. 3.4. The susceptibility is normalized by $\nu(E_f) = 2E_f/\pi n u_F^2$, where E_f is the Fermi energy. The x-axis is normalized using the Fermi wave number, ($k_F = \sqrt{n\pi}$) with n being the electron density. The electron density is related to the chemical potential (for more information refer to Ref. [61]). Fig. 3.4 shows a great agreement between the data in Ref .[61] and the result obtained using the Lindhard code developed in the present study.

3.2.3 NFRHT

In order to ensure that the exchange functions Z_E.m and Z_P.m (refer to Fig. 3.1) and the NFRHT codes are implemented correctly, another verification is necessary. The results obtained using these two functions are compared with the data presented in Messina et al. [65] to ensure the accuracy of these MATLAB functions. The data presented in Messina et al. [65] is concerned with the total near-field heat flux between a zinc sulfide (ZnS) slab, kept at a temperature of 290 K, and a gallium arsenide (GaAs) slab that is kept at a temperature of 310 K (refer to Fig.3.5). A 10 nanometers vacuum gap separates the two slabs. Heat transfer in this system is studied for two cases. In the first case the GaAs slab is not covered with a graphene sheet while in the second case it is covered with a graphene sheet. In the study by Messina et al., the calculated electrical conductivity of graphene is modeled using the Kubo formulation.

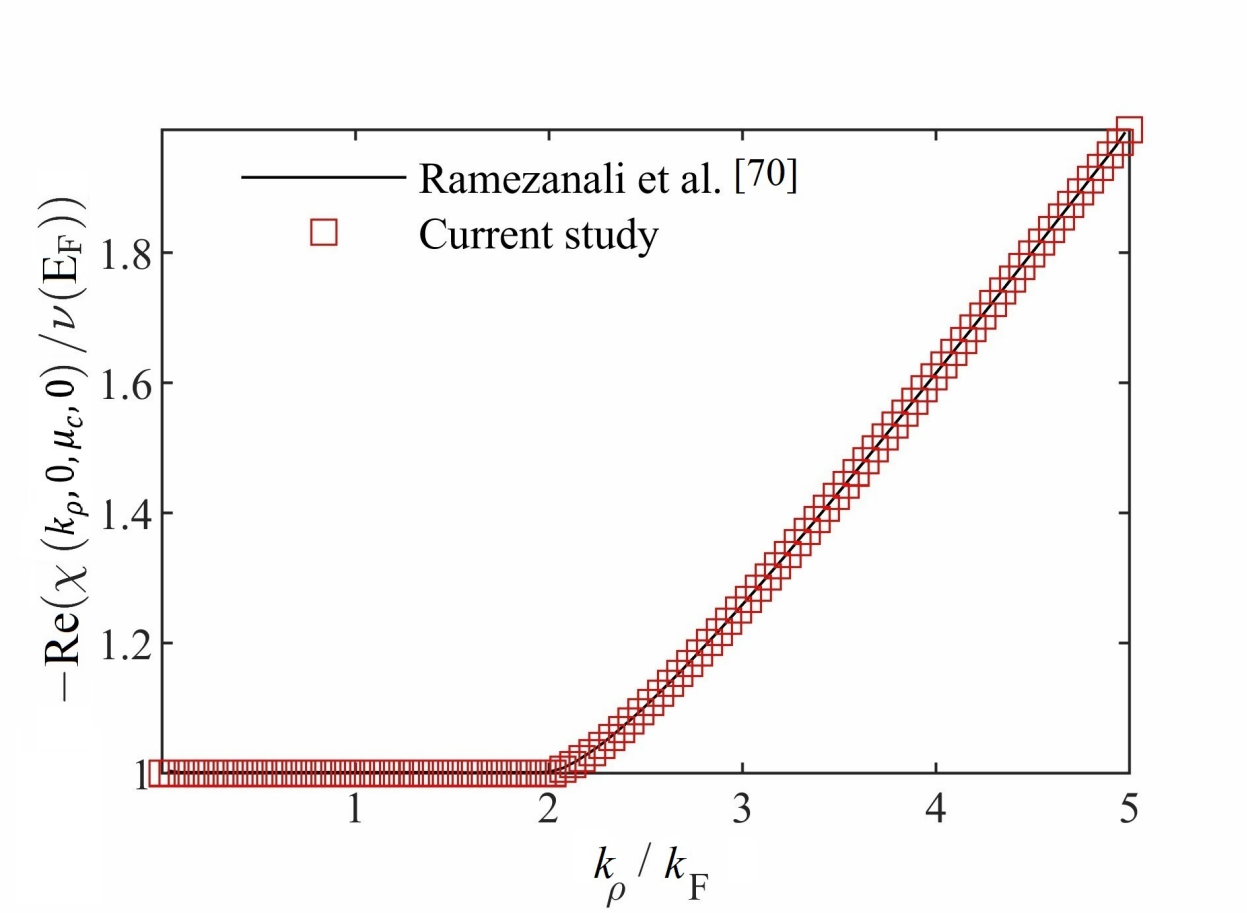

Figure 3.4. Verification of the Lindhard code against the data presented in Ref. [70] for $T = 0$ K and $\omega = 0$ rad/s.

To determine the frequency range in which thermal radiation is non-negligible, first the total heat flux is computed in the frequency range of $1.88 \times 10^{12} rad/s$ to 1.88×10^{17} rad/s. Then we reduced the upper limit to 1.88×10^{16} rad/s and increased the lower limit to 1.88×10^{14} rad/s until no change in the radiative heat flux was observed. The total (spectrally integrated) heat transfer is integrated numerically over the frequency. To ensure the convergence of the numerical integral, the number of frequencies used for discretizing a given frequency range was increased until no change in the total heat flux is observed. The convergence analysis data are summarized in Table 3.1.

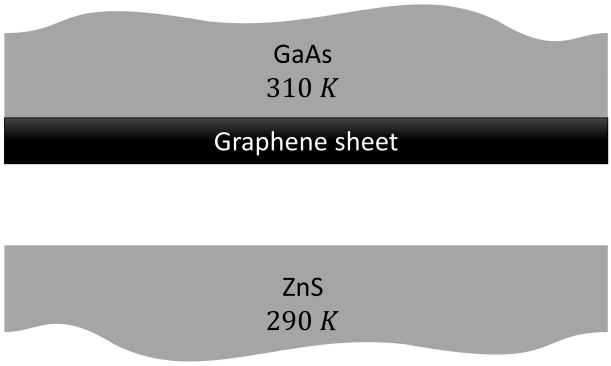

Figure 3.5. Near-field radiative heat transfer between a GaAs slab at 310 K and a ZnS slab at 290 K. The GaAs slab is covered with a graphene sheet

Table 3.1. Frequency range and frequency count dependency analysis on near-field heat flux between graphene covered GaAs at $T = 310K$ and ZnS at $T = 290K$.

ω_{max} [rad/s]	ω_{min} [rad/s]	Frequency count	$q''_{total}[W/m^2]$
1.88×10^{16}	1.88×10^{15}	500	3.95×10^3
1.88×10^{16}	1.88×10^{15}	1000	3.95×10^3
1.88×10^{16}	1.88×10^{15}	2000	3.95×10^3
1.88×10^{16}	1.88×10^{14}	500	4.39×10^3
1.88×10^{16}	1.88×10^{14}	1000	4.27×10^3
1.88×10^{16}	1.88×10^{14}	4000	4.24×10^3
1.88×10^{16}	1.88×10^{14}	10000	4.24×10^3
1.88×10^{16}	1.88×10^{13}	1000	4.56×10^3
1.88×10^{16}	1.88×10^{13}	10000	4.27×10^3
1.88×10^{16}	1.88×10^{13}	20000	4.25×10^3
1.88×10^{17}	1.88×10^{12}	1000	6.25×10^2
1.88×10^{17}	1.88×10^{12}	10000	6.09×10^3
1.88×10^{17}	1.88×10^{12}	100000	4.27×10^3

It is seen from Table 3.1 that radiative heat transfer between the slabs is only non-negligible in the frequency range of $1.88 \times 10^{14} rad/s$ to $1.88 \times 10^{16} rad/s$. Additionally, Table 3.1 shows that dividing the frequency range into 4000 sub-intervals is sufficient. The total heat transfer versus the chemical potential is presented in Messina et al. [65] is shown in Fig. 3.6.

As it is seen from Fig. 3.6, the results obtained using the implemented codes match the ones presented in Messina et al. [65]. Therefore, developed codes are verified. Now the focus shall be shifted toward presenting the results.

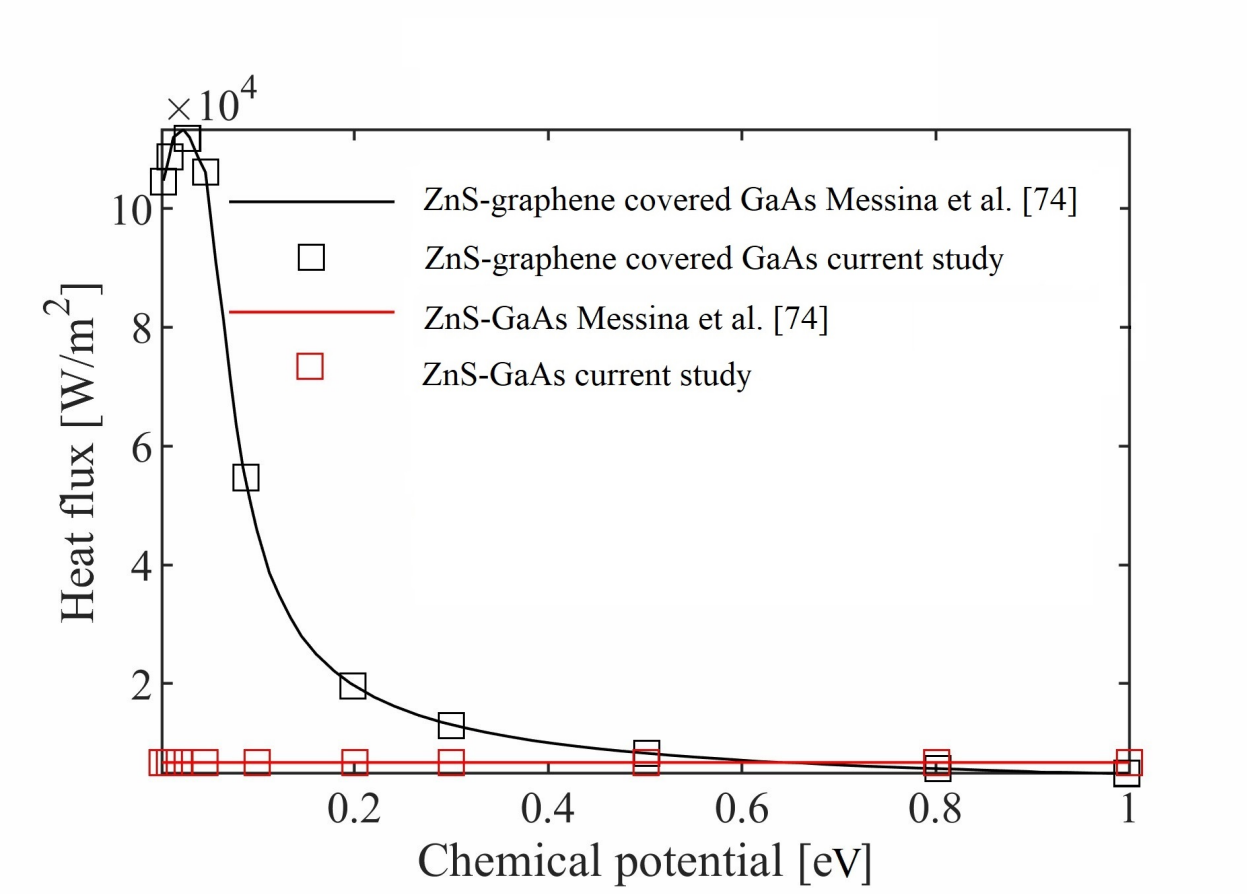

Figure 3.6. Total radiative heat flux between graphene covered GaAs-ZnS and bare GaAs-ZnS separated by a 10 nm vacuum gap, as a function of chemical potential using Kubo formula separated.

3.3 Results

In this section, the electrical conductivity of graphene is calculated using both the Kubo and Lindhard formulas, and the Kubo and Lindhard electrical conductivities are compared. Then the radiative conductance obtained by these models are compared for various conditions and finally, the effect of gap size and temperature on radiative conductance is discussed.

3.3.1 Comparison of Kubo and Lindhard methods: Electrical Conductivity

The conductivity of graphene is calculated using the Kubo (Eq. 2.24) and Lindhard (Eqs. 2.28 and 2.29) formulas. In order to compare the two methods, the conductivity of a single graphene sheet at $T = 300$ K is calculated using both methods in the frequency range of 5×10^{11} rad/s to 5×10^{14} rad/s. The frequency and wavevector dependant colorplots of graphene's conductivity at $\mu_c = 0.1$ eV and 0.3 eV are shown in Fig. 3.7 and 3.8, respectively. In Fig. 3.7 and 3.8, panels (a) and (c) are calculated using the Lindhard formula, while panels (b) and (d) are found by using the Kubo formula. Panels (a) and (b) show the imaginary part of the electrical conductivity of graphene, while panels (c) and (d) show the real part of it.

Figures 3.7 and 3.8 show that graphene's conductivity obtained using the Lindhard formula is a function of wavevector (k_ρ), while the Kubo electrical conductivity doesn't depend on the wavevector. As the wavevector increases, the imaginary part of Lindhard electrical conductivity at higher frequencies increases. However, this variation is not captured by the Kubo formula. Similar trend is observed from the comparison of the imaginary part of graphene's Kubo and Lindhard conductivities at $T = 300$ K and $\mu_c = 0.3$ eV (refer to Fig. 3.8.a and 3.8.b).

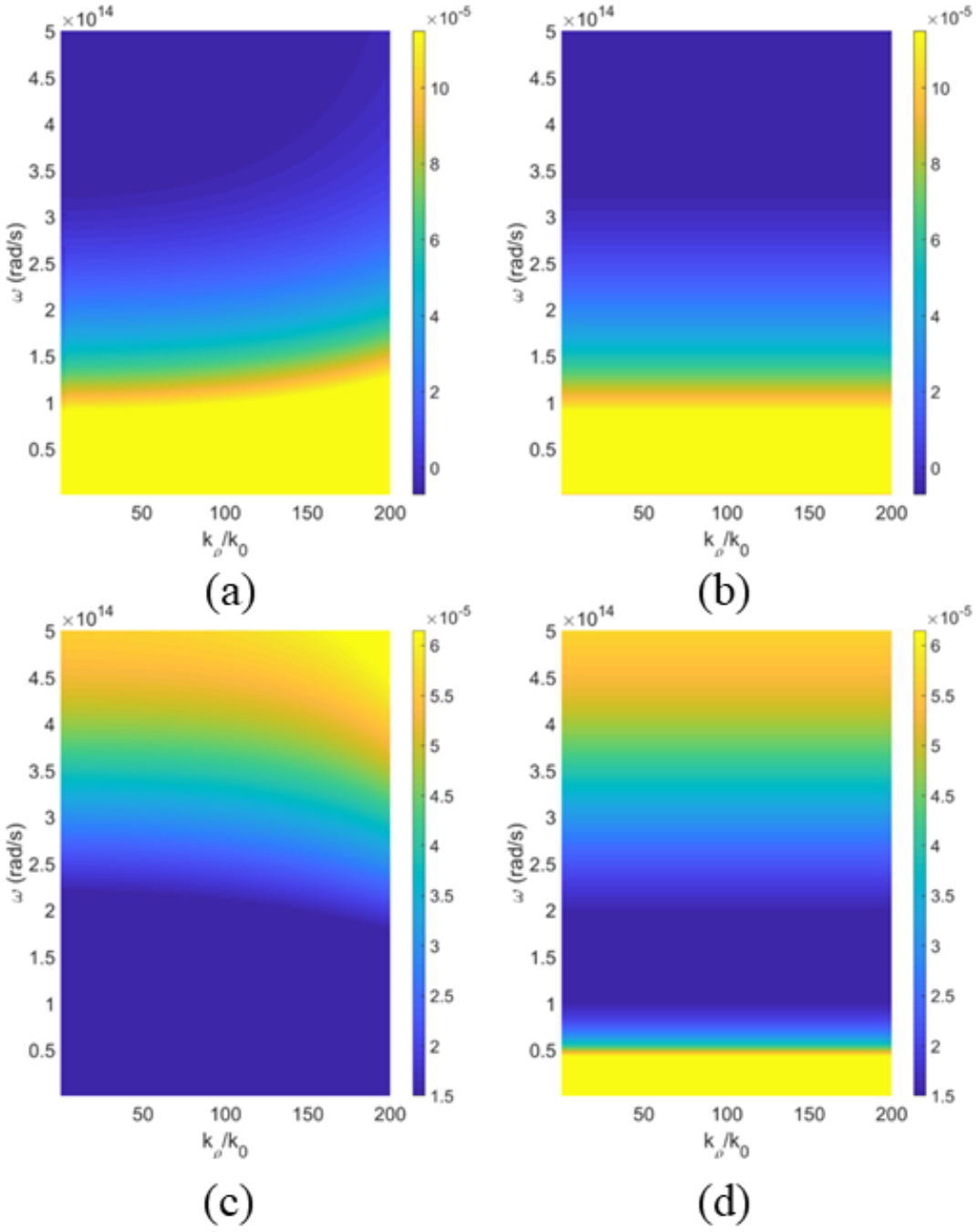

Figure 3.7. Graphene's electrical conductivity at $\mu_c = 0.1$ eV in frequency range 5×10^{11} rad/s to 5×10^{14} rad/s at $T = 300$ K. Panels (c), (a), (d) and (b) show the real and imaginary parts of the Kubo electrical conductivity and the real and imaginary parts of the Lindhard electrical conductivity, respectively.

Comparison of the real part of the Kubo and Lindhard electrical conductivity at $T = 300$ K and $\mu_c = 0.1$ eV (refer to Fig. 3.7.c and 3.7.d) presented in Figs. 3.7.c and 3.7.d also show that graphene's conductivity by the Lindhard formula is a function of wavevector whereas the Kubo one is not. Another observation from these figures is that graphene's electrical conductivity calculated using the Kubo formula at small frequencies ($\omega < 6 \times 10^{13}$ rad/s) is almost 6 folds that calculated by the Lindhard formula. Similar observation are made from Fig. 3.8.c and 3.8.d for $\mu_c = 0.3$ eV at T = 300 K, where at $\omega < 4 \times 10^{13}$ rad/s there is almost an order of magnitude difference in the electrical conductivity calculated using the Kubo and Lindhard formulas. Both methods agree at zero to small wavevectors for $\omega < 6 \times 10^{13}$ rad/s.

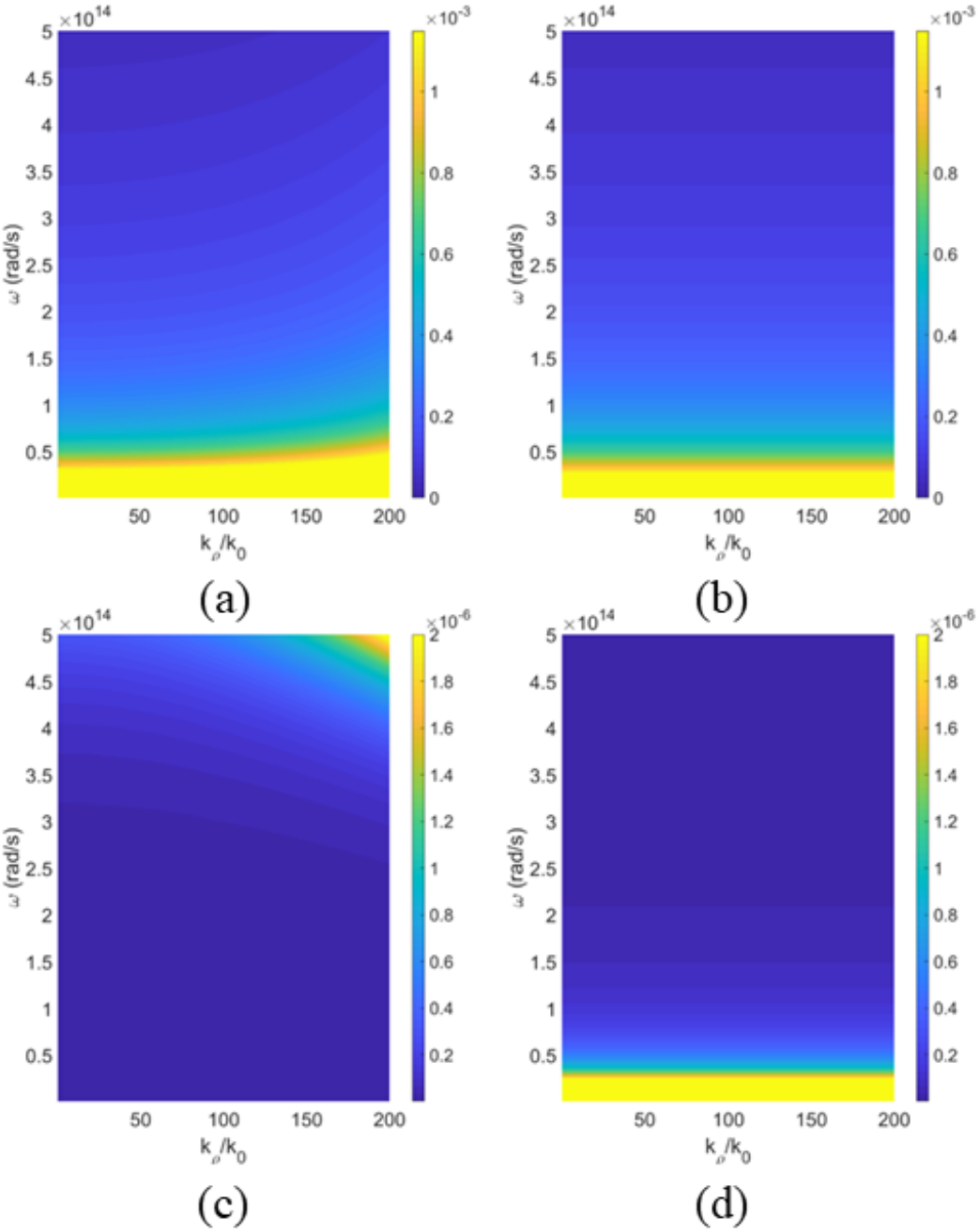

Figure 3.8. Graphene's electrical conductivity at $\mu_c = 0.3$ eV in frequency range 5×10^{11} rad/s to 5×10^{14} rad/s at $T = 300$ K. Panels (c), (a), (d) and (b) show the real and imaginary parts of the Kubo electrical conductivity and the real and imaginary parts of the Lindhard electrical conductivity, respectively.

3.3.2 Comparison of Kubo and Lindhard methods: Radiative conductance

In this section, the radiative conductance (refer to Eq. 2.21) between two free-standing graphene sheets at T = 300 K separated by a vacuum gap of size D = 50 nm is calculated using both the Kubo and Lindhard formulas. The schematic of the problem is shown in Fig. 3.9. The radiative conductance per unit frequency and wavevector is plotted versus ω and k_ρ/k_0 in Fig. 3.10 for various chemical potential values (μ_c). The spatial dispersion of graphene plasmons are also shown in this figure as well. In Fig. 3.10, panels (a), (b), (c) and (d) are found using the Lindhard function while panels (e), (f), (g) and (h) are found using the Kubo formula. Fig. 3.10.a and e are for $\mu_c = 0.05$ eV, Fig. 3.10.b and f are for $\mu_c = 0.1$ eV, Fig. 3.10.c and g are for $\mu_c = 0.3$ eV and Fig. 3.10.d and h are for $\mu_c = 0.5$ eV.

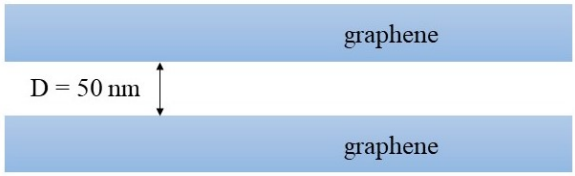

Figure 3.9. Schematic of the problem under study. Two graphene sheets at T = 300 K are separated by a 50 nm vacuum gap.

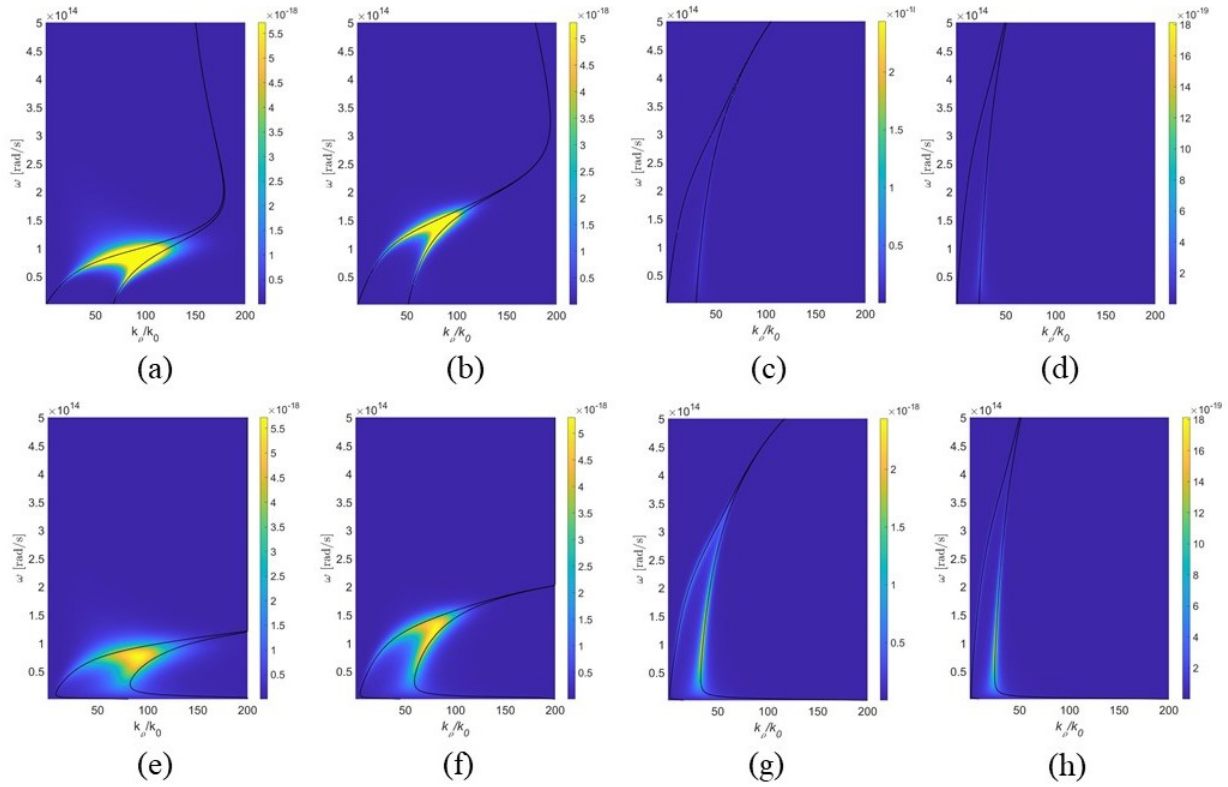

Figure 3.10. Radiative conductance versus ω and k_ρ/k_0 at $T = 300$ K and $D = 50$ nm. Panels a ($\mu_c = 0.05$ eV), b (0.1 eV), c (0.3 eV) and d (0.5 eV) are calculated using Lindhard formula while panels e ($\mu_c = 0.05$ eV), f (0.1 eV), g (0.3)eV and h (0.5 eV) are found using the Kubo formula.

It can be seen from Fig. 3.10 that there is non-negligible differences between the radiative conductance and dispersion relation as obtained using the Kubo and Lindhard electrical conductivities. The difference between the Kubo and Lindhard radiative Conductance is particularly significant around the dispersion relation of graphene's surface plasmons.

The difference between radiative conductance obtained using the Lindhard formula and the one found using the Kubo formula is smaller at smaller values of chemical potential. As the chemical potential increases, the bright bands (corresponds to higher radiative conductance) obtained using the Lindhard formula fade. At the same time, the Kubo

formula still exhibits sharp detectable bright bands at $\mu_c = 0.3$ eV and 0.5 eV. The quantity of interest in NFRHT is the spectral radiative conductance that is found by integrating the radiative conductance over k_ρ. The spectral radiative conductance between two graphene sheets at $T = 300$ K separated by a gap of size $D = 50$ nm is plotted in Fig. 3.11. Figure 3.11.a is obtained by using the Kubo formula, and Fig. 3.11.b is obtained by using the Lindhard formula. It can be seen that as the chemical potential increases, the peak frequency, which corresponds to thermal excitation of graphene's SPPs shifts toward higher frequencies.

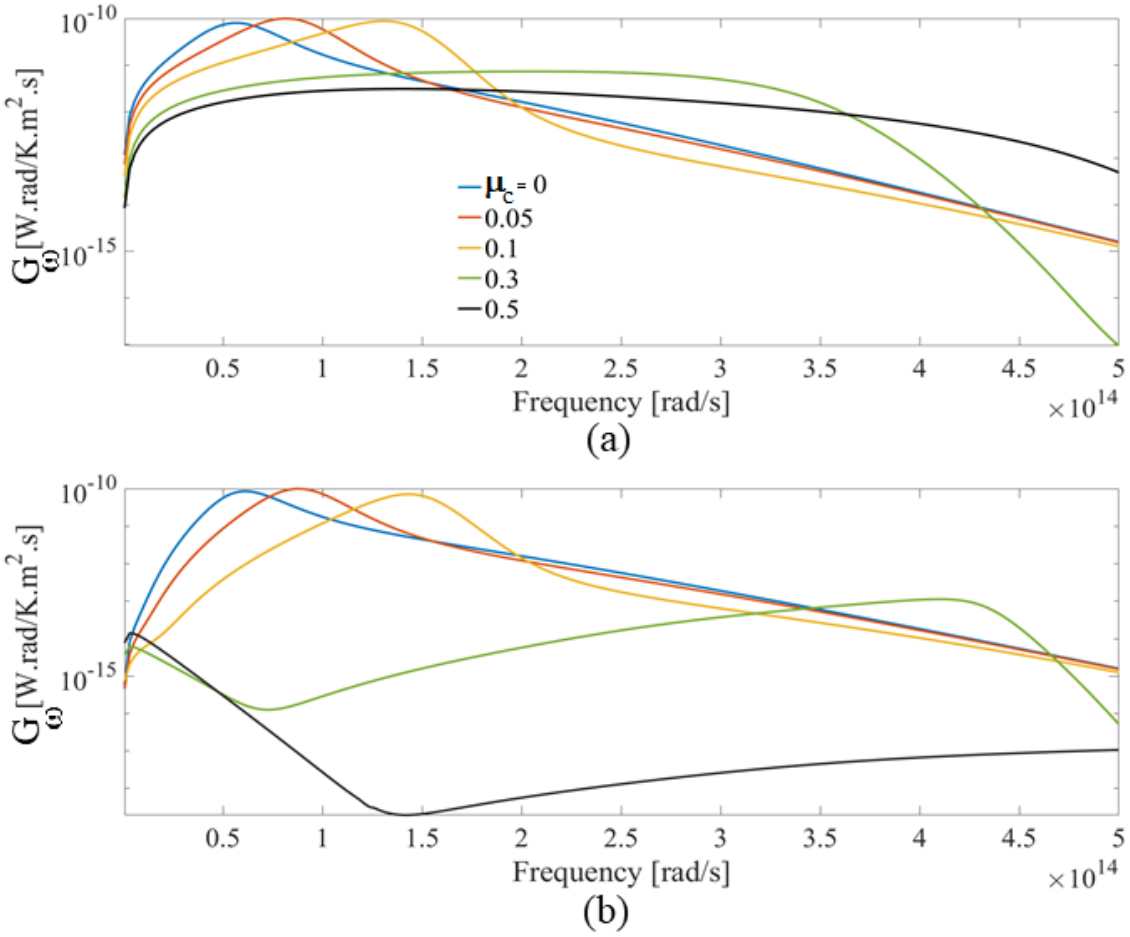

Figure 3.11. Spectral radiative conductance between two graphene sheets at $T = 300$ K separated by a gap of $D = 50$ nm for different chemical potentials calculated using (a) Kubo formula and (b) Lindhard formula.

The spectral radiative conductance ontained using the Kubo and Lindhard formula are compared in Fig. 3.12 for $T = 300$ K, $D = 50$ nm and at different chemical potentials. Fig. 3.12.a is for $\mu_c = 0.05$ eV, Fig. 3.12.b is for $\mu_c = 0.1$ eV, Fig. 3.12.c is for $\mu_c = 0.3$ eV and Fig. 3.12.d is for $\mu_c = 0.5$ eV.

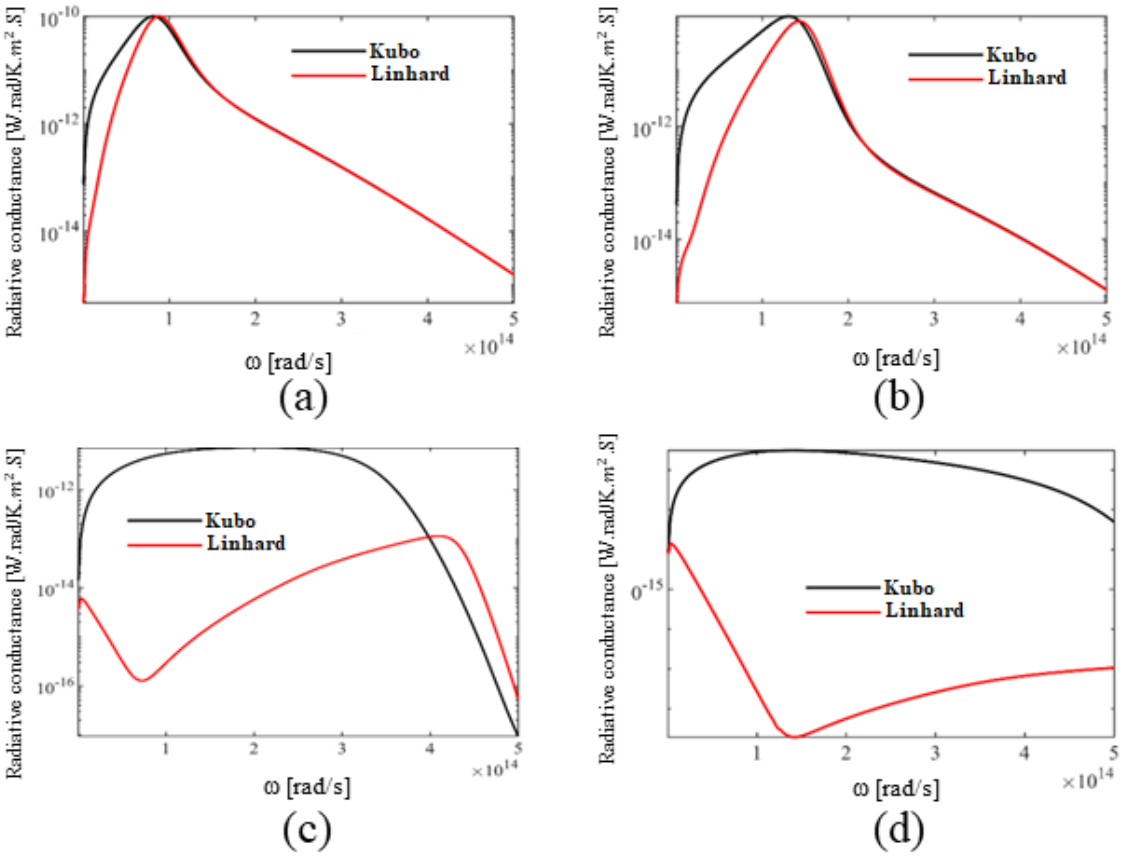

Figure 3.12. Spectral radiative conductance between two graphene sheets at $T = 300$ K separated by a gap size of $D = 50$ nm for different chemical potentials of (a) $\mu_c = 0.05$, (b) 0.1, (c) 0.3 and (d) 0.5 eV.

It can be seen from Fig. 3.12 that the peak of radiative conductance experiences a blueshift as the chemical potential of the graphene increases. The radiative conductance calculated using the Kubo and Lindhard methods shows great agreement at $\mu_c = 0.05$ eV and 0.1 eV for high frequencies (for $\mu_c = 0.05$ eV the agreement region is $\omega > 10^{14}$ rad/s and it is $\omega > 1.5 \times 10^{14}$ rad/s for $\mu_c = 0.1$ eV). Another observation is that at chemical

potentials of 0.3 eV and 0.5 eV, the Kubo formula estimates a broadband radiative conductance while there is a well-defined plasmon resonance in the conductance curve using the Lindhard formula. It is also seen that at large values of graphene's chemical potential, the Kubo formula overestimates the radiative conductance. This shows that the non-local effects of electrical conductivity cannot be ignored for large values of chemical potential.

A quantitative comparison between the total radiative heat flux using the Kubo and Lindhard formulas for two graphene sheets at $T_1 = 300$ K and $T_2 = 290$ K, separated by a 50 nm vacuum gap, is provided in Fig. 3.13.

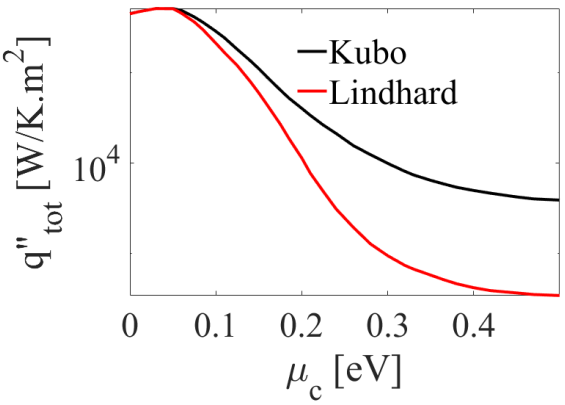

Figure 3.13. Total radiative heat flux between graphene sheets at $T_1 = 300$ K and $T_2 = 290$ K separated by a vacuum gap of D = 50 nm as a function of chemical potential.

The total heat flux presented in Fig. 3.13 shows the effects of chemical potential on the agreement of Kubo formula and Lindhard formulas. It can be seen that both methods agree for chemical potentials less than 0.05 eV. For $\mu_c = 0.1$ eV, there is a 25% difference, and the difference grows to an order of magnitude for $\mu_c = 0.5$ eV. Fig. 3.13 shows that at large chemical potentials, the Kubo formula overestimates NFRHT significantly.

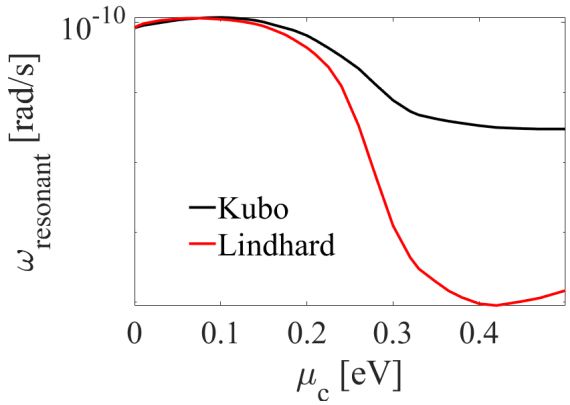

Figure 3.14. Peak frequency of radiative conductance between two graphene sheets at $T = 300$ K, separated by a gap of $D = 50$ nm versus μ_c.

The effect of changing chemical potential of graphene sheets on peak frequency of radiative conductance in the problem shown in Fig. 3.9 is studied in Fig. 3.14. Fig. 3.14 shows that at chemical potential smaller than 0.15 eV, the difference is less than 15%. This difference increases by increasing the chemical potential up to $\mu_c = 0.42$ eV, where the difference is two orders of magnitude. Fig. 3.14 shows a reduction in the difference of the peak frequency of radiative conductance found using the Kubo and Lindhard formulas above $\mu_c = 0.42$ eV. It can be concluded that the Kubo formula can be used for predicting the peak frequency for chemical potentials up to $\mu_c = 0.15$ eV under the studied conditions, and the Kubo results above $\mu_c = 0.15$ eV deviate too much from the Lindhard ones.

3.3.3 Effect of temperature and gap size on radiative conductance and peak frequency

In this subsection, the effect of temperature and gap size on radiative conductance and the peak or resonant frequency of the radiative conductance are studied. First the effect of gap size on the radiative conductance is studied for $\mu_c = 0.2$ eV and $T = 300$ K. Figure 3.15.a shows the radiative conductance for the Kubo formula while Fig. 3.15.b shows the same for the Lindhard formula. It can be seen that both methods predict that by

increasing the gap size, the spectral radiative conductance decreases and the peak frequency of the spectral radiative conductance shifts toward smaller frequencies.

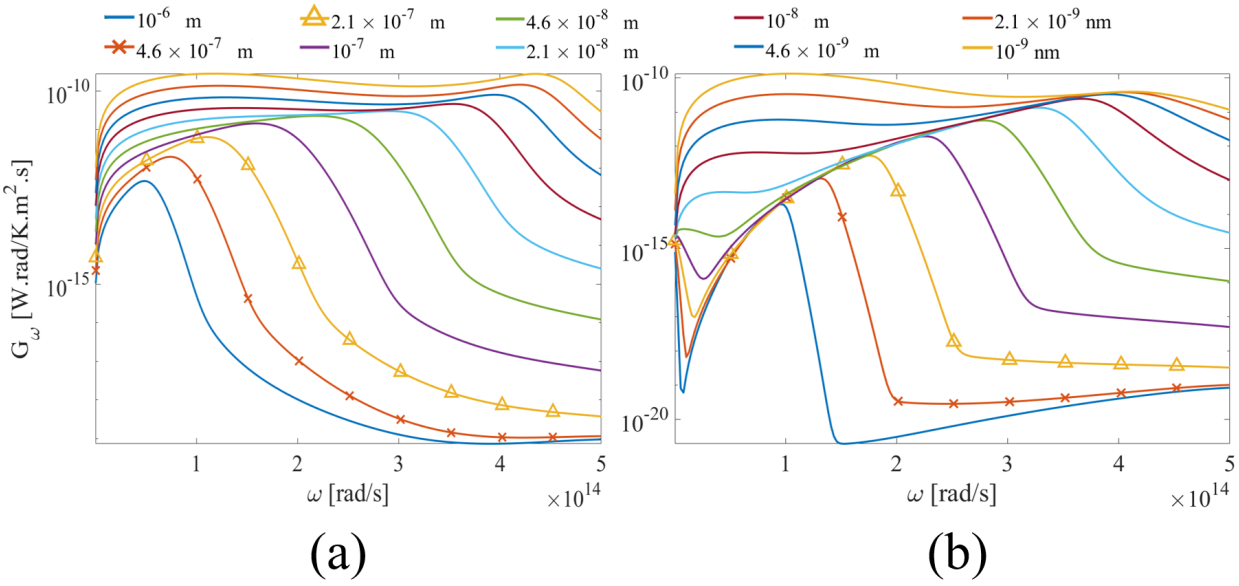

Figure 3.15. Spectral radiative conductance between two graphene sheets at T = 300 K and $\mu_c = 0.2$ eV at different gap sizes as calculated using (a) the Kubo formula and (b) the Lindhard formula.

In order to understand the effect of gap size on the agreement of the Kubo and Lindhard formulas for predicting the resonant frequency of radiative conductance, the resonant frequency of radiative conductance versus gap size is plotted in Fig. 3.16. It is shown in Fig. 3.16 that at $D < 10^{-8}$ m, the resonant frequency obtained using both Kubo and Lindhard are very close (less than 3% difference), and by increasing the gap size, the resonant frequency estimated by Kubo and Lindhard formulas diverge to a point that at $D = 10^{-6}$ m and $D = 4.6 \times 10^{-7}$ m, the relative difference is about 49% and 42%, respectively. Hence increasing the gap size deteriorates Kubo formula's ability to predict the resonant frequency correctly. Another observation from Fig. 3.16 is that by increasing the gap size, both methods predict that the resonant frequency shifts to lower frequencies.

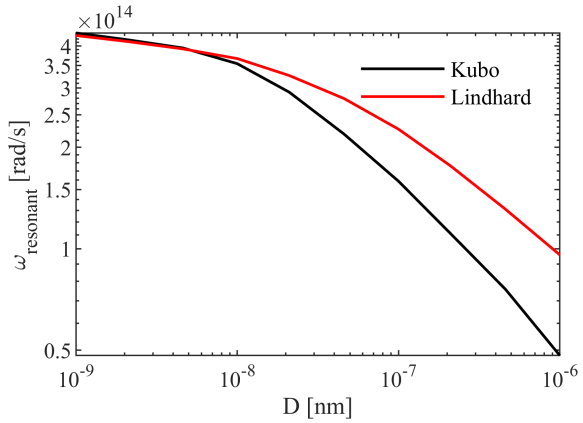

Figure 3.16. Resonant frequency of the radiative conductance of two graphene sheets at T = 300 K and $\mu_c = 0.2$ eV versus gap size, D.

Total radiative conductance between graphene sheets at $T = 300$ K and $\mu_c = 0.2$ eV is plotted versus gap size, D, in Fig. 3.17. Figure 3.17 shows that there is a 90% difference in the total radiative conductance calculated using the Kubo and Lindhard formulas at gap sizes ($D > 10^{-7}$ m), and this difference reduces to 60% as the gap size reduces to $D = 10^{-8}$ m and about 30% for $D = 10^{-9}$. This shows that the overestimation of total radiative conductance using the Kubo formula increases as the gap size increase.

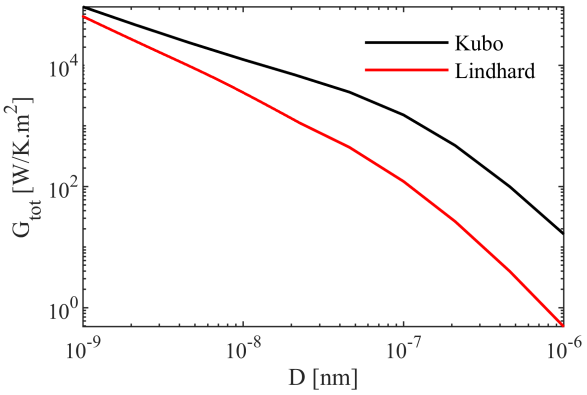

Figure 3.17. Total radiative conductance between two graphene sheets at T = 300 K and $\mu_c = 0.2$ eV versus gap size, D.

The effect of temperature on radiative conductance between two graphene sheets with $\mu_c = 0.2$ eV that are placed 50 nm apart is studied using the Kubo formula in Fig. 3.18.a and the Lindhard formula in Fig. 3.18.b. It can be seen that increasing the temperature from 100 K to 1000 K shifts the resonant frequency of radiative conductance to lower frequencies and increases the radiative conductance significantly.

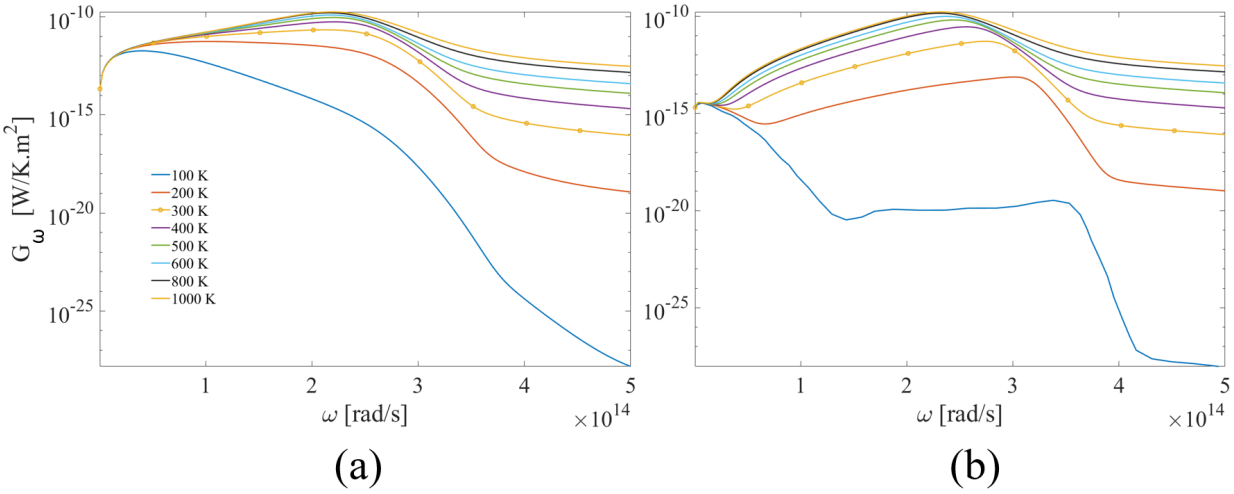

Figure 3.18. Spectral radiative conductance between two graphene sheets at $D = 50$ nm and $\mu_c = 0.2$ eV at different temperatures as calculated (a) using the Kubo formula and (b) Lindhard formula.

The resonant frequency of the radiative conductance versus temperature is plotted in Fig. 3.19. It can be seen that the resonant frequency obtained using the Kubo formula is 4.1×10^{13} rad/s for $T = 100$ K, and it increases to 2.43×10^{14} rad/s for $T = 380$ K. As the temperature increases further, the resonant frequency slightly decrease, such that it is equal to 2.22×10^{14} rad/s at $T = 1000$ K. On the other hand, the Lindhard formula predicts a decrease in the resonant frequency as temperature increases from 100 K to 1000 K.

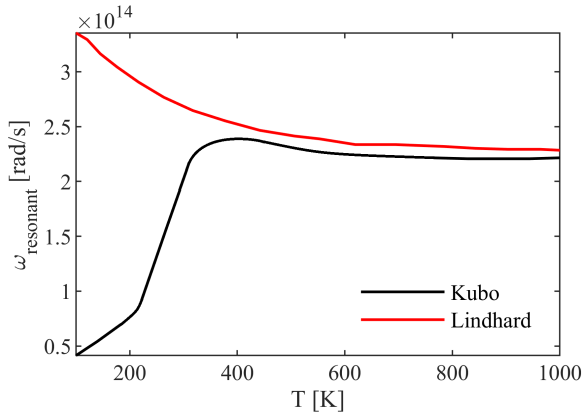

Figure 3.19. Resonant frequency of radiative conductance of two graphene sheets at $\mu_c = 0.2$ eV separated by a vacuum gap of size D = 50 nm versus temperature, T.

The total radiative conductance between graphene sheets versus the temperature is plotted in Fig. 3.20. Figure 3.20 shows that when $T < 200$ K, there is two orders of magnitude difference between the results obtained using the Kubo and Lindhard formulas. This difference reduces to almost 20% when 600 K $< T <$ 800 K and finally reaches 6% at $T = 1000$ K. Hence, Fig. 3.20 shows that as the temperature of graphene sheets grows, the result of the Kubo and Lindhard formulas converge. Figure 3.20 and 3.19 show that the Kubo formula does not provide a suitable representation for graphene sheets in NFRHT applications at temperatures less than 400 K.

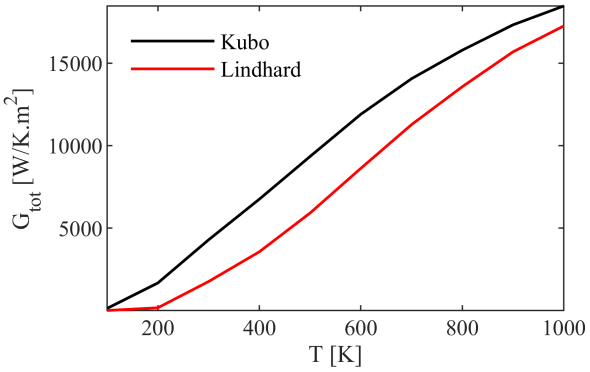

Figure 3.20. Total radiative conductance between two graphene sheets at $\mu_c = 0.2$ eV separated by a vacuum gap of size D = 50 nm versus temperature, T.

The results presented in this chapter shows that graphene is a non-local material whose properties can be tuned significantly by changing its chemical potential. The Kubo formula, which is a local model for graphene's electrical conductivity, cannot capture the non-local behavior of graphene at low temperatures and high chemical potentials, and applying the Kubo formula under these conditions causes significant errors. To avoid this error, the Lindhard formula should be used for modeling graphene's electrical conductivity in NFRHT calculations.

CHAPTER 4
CONCLUSIONS, FUTURE WORK AND RECOMMENDATIONS

4.1 Conclusions

This thesis investigates the non-locality of graphene's electrical conductivity and the non-local effects of electrical conductivity on near-field radiative heat transfer (NFRHT). In NFRHT studies found in literature, graphene electrical conductivity has been modeled using a local model (Kubo formula). To study the effect of non-local electrical conductivity of graphene on NFRHT, the near-field radiative conductance between two suspended graphene sheets separated by a vacuum gap has been modeled using the Kubo formula and a non-local model, namely, the Lindhard formula. For this system of two graphene sheets, the electrical conductivity of graphene for various wavevectors and frequencies, the wavevector dependent spectral radiative conductance, spectral and total radiative conductance, resonant frequency as well as dispersion relation have been studied. The effect of temperature and gap size on applicability of the local model of graphene's electrical conductivity has also been studied.

Comparing the spectral radiative conductance (Fig. 3.11 and 3.12) and total heat flux versus chemical potential (Fig. 3.13) as obtained using the Kubo and Lindhard formulas showed that as the chemical potential (μ_c) of graphene increases, the disagreement of the two models increases. It was shown that for $\mu_c < 0.1$ eV, there is less than 25% difference in the total heat flux of the two models. the difference grows to an order of magnitude as chemical potential increases to $\mu_c = 0.5$ eV. The same observation was made for the resonant frequency versus chemical potential (Fig. 3.14), where it was found that at $\mu_c < 0.15$ eV, the resonant frequency predicted by the local and non-local models is only 15% and the difference increases significantly by increasing the chemical potential of the graphene sheets. These findings show that the non-local effects of graphene's electrical

conductivity play a significant role when $\mu_c > 0.1$ eV, and hence using the Kubo formula can result in non-negligible errors.

The difference between the resonant frequency and the total radiative conductance of the two graphene sheets was also been studied for various gap sizes (Fig. 3.16 and refgtotgap). It was seen that as the gap size grows, the Kubo formula fails more to predict a resonant frequency of radiative conductance which is reasonably close to the one obtained by using the Lindhard formula. For example, at $D < 10^{-8}$ m, the difference is only 3%. However, the difference increases to 49% at $D = 10^{-6}$ m. It was also shown that decreasing the gap size from 10^{-7} m to 10^{-9} m, at $\mu_c = 0.2$ eV and $T = 300$ K, reduces the difference of the total radiative conductance obtained using the two methods. The difference between the two models is 60% at $D = 10^{-8}$. Therefore, the Kubo formula is invalid at large separation gaps.

Comparison of resonant frequency (Fig. 3.19) and the total radiative conductance (Fig. 3.20) for various temperatures showed that as the temperature increases, the difference between the two models decreases. It was seen that when $T > 400$ K, the resonant frequency obtained using both models are less than 7% apart. The difference between the total radiative conductance for $T < 200$ K is about two orders of magnitude different, and this difference reduces to 20% for $T > 600$ K. Therefore, the Kubo model cannot fully capture the non-local behavior of graphene's electrical conductivity at low temperatures and hence the Kubo formula is not suggested for NFRHT applications in this temperature range.

Based on the fact that the Kubo formula is not applicable at large values of chemical potential and separations gaps as well as at low temperatures, it is recommended that the non-local behavior of graphene's electrical conductivity be considered in NFRHT application. The Lindhard formula can capture the non-local effects on the electrical

conductivity of graphene. It should be mentioned that the computational cost of the Lindhard formula is only slightly higher than the Kubo formula.

4.2 Future Work and Recommendations

Graphene is a very promising material for NFRHT applications as if support tunable surface plasmon polaritons in the infrared. In this thesis we showed that the effect of non-local electrical conductivity on graphene's NFRHT is non-negligible and should be taken into account. Some recommendations for future work are presented hereafter.

1. Experimentally demonstrate that non-local effects affect NFRHT in graphene-based materials. Total heat transfer can be measured and compared with the theoretical predictions using the Kubo and Lindhard formulas.

2. It is shown that if graphene substrate supports surface phonon polaritons (such as SiO_2 and SiC), the graphene SPPs can be coupled to the SPhPs of the substrate. This coupling can result in enhancement and tunability of NFRHT. It is recommended to study if such coupling, enhancement and tuning are observed when non-local effects of the electrical conductivity are considered.

3. Graphene has been proposed as a base material for designing metamaterials such as hyperbolic metamaterials and magneto-dielectric metamaterials. It is recommended to study how the non-local electrical conductivity of graphene can affect thermal radiation of the proposed metamaterial.

5. It is recommended that the effect of non-local electrical conductivity on NFRHT in other two-dimensional materials, such as black phosphorene, that have been proposed for near-field applications be analyzed.

REFERENCES

[1] Willy Wien. On the division of energy in the emission-spectrum of a black body. *The London, Edinburgh, and Dublin Philosophical Magazine and Journal of Science*, 43(262):214–220, 1897.

[2] Roberto Mauri. Radiant heat transfer. *Transport Phenomena in Multiphase Flows*, 112:339–352, April 2015.

[3] Max Planck. *The theory of heat radiation*. Dover Publications, 1991.

[4] Edgar Meyhofer Bai Song, Anthony Fiorino and Pramod Reddy. Near-field radiative thermal transport: From theory to experiment. *AIP Advances*, 5(5):053503, May 2015.

[5] Mario Bertolotti, Concita Sibilia, and Angela M. Guzman. *Evanescent Waves in Optics*. Springer International Publishing, 2017.

[6] Karl Joulain, Jean-Philippe Mulet, Francois Marquier, Rémi Carminati, and Jean-Jacques Greffet. Surface electromagnetic waves thermally excited: Radiative heat transfer, coherence properties and casimir forces revisited in the near field. *Surface Science Reports*, 57(3-4):59–112, May 2005.

[7] Jean-Philippe Mulet, Karl Joulain, Rémi Carminati, and Jean-Jacques Greffet. Enhanced radiative heat transfer at nanometric distances. *Microscale Thermophysical Engineering*, 6(3):209–222, July 2002.

[8] Jean-Philippe Mulet, Karl Joulain, Remi Carminati, and Jean-Jacques Greffet. Nanoscale radiative heat transfer between a small particle and a plane surface. *Applied Physics Letters*, 78(19):2931–2933, May 2001.

[9] Jean-Jacques Greffet, Remi Carminati, Karl Joulain, Jean-Philippe Mulet, Stephane Mainguy, and Yong Chen. Coherent emission of light by thermal sources. *Nature*, 416(6876):61–64, March 2002.

[10] L. Novotny A. J. Huber, B. Deutsch and R. Hillenbrand. Focusing of surface phonon polaritons. *Applied Physics Letters*, 92(20):203104, 2008.

[11] Anatoly V. Zayats, Igor I. Smolyaninov, and Alexei A. Maradudin. Nano-optics of surface plasmon polaritons. *Physics Reports*, 408(3-4):131–314, March 2005.

[12] C. R. Williams, S. R. Andrews, S. A. Maier, A. I. Fernandez-Dominguez, L. Martin-Moreno, and F. J. Garcia-Vidal. Highly confined guiding of terahertz surface plasmon polaritons on structured metal surfaces. *Nature Photonics*, 2(3):175–179, February 2008.

[13] Duong Thi Ha, Dinh Thi Thuy, Vo Thi Hoa, Tran Thi Thanh Van, and Nguyen Ai Viet. On the theory of three types of polaritons (phonon, exciton and plasmon polaritons). *Journal of Physics: Conference Series*, 865:012007, June 2017.

[14] Herbert B. Callen and Theodore A. Welton. Irreversibility and generalized noise. *Phys. Rev.*, 83(1), 1951.

[15] D. Polder and M. Van Hove. Theory of radiative heat transfer between closely spaced bodies. *Physical Review B*, 4(10):3303–3314, November 1971.

[16] Serge Mikhalovich Rytov. Theory of electric fluctuations and thermal radiation. *USSR Academy of Sciences Press*, 1953.

[17] Jose Meseguer, Isabel Perez-Grande, and Angel Sanz-Andres. Thermal radiation heat transfer. In *Spacecraft Thermal Control*, pages 73–86. Elsevier, 2012.

[18] A. G. Emslie. Radiation transfer by closely spaced shields. *Arthur D. Little Inc.*, 1961.

[19] E. G. Cravalho, C. L. Tien, and R. P. Caren. Effect of small spacings on radiative transfer between two dielectrics. *Journal of Heat Transfer*, 89(4):351–358, November 1967.

[20] G. A. Domoto and C. L. Tien. Thick film analysis of radiative transfer between parallel metallic surfaces. *Journal of Heat Transfer*, 92(3):399–404, August 1970.

[21] F. Singer, Y. Ezzahri, and K. Joulain. Nonlocal study of the near field radiative heat transfer between two n-doped semiconductors. *International Journal of Heat and Mass Transfer*, 90:34–39, November 2015.

[22] Geoff Wehmeyer, Tomohide Yabuki, Christian Monachon, Junqiao Wu, and Chris Dames. Thermal diodes, regulators, and switches: Physical mechanisms and potential applications. *Applied Physics Reviews*, 4(4):041304, December 2017.

[23] Hideo Iizuka and Shanhui Fan. Rectification of evanescent heat transfer between dielectric-coated and uncoated silicon carbide plates. *Journal of Applied Physics*, 112(2):024304, July 2012.

[24] Arvind Narayanaswamy and Gang Chen. Surface modes for near field thermophotovoltaics. *Applied Physics Letters*, 82(20):3544–3546, May 2003.

[25] M Francoeur, R Vaillon, and M Pinar Menguc. Thermal impacts on the performance of nanoscale-gap thermophotovoltaic power generators. *IEEE Transactions on Energy Conversion*, 26(2):686–698, June 2011.

[26] Anthony Fiorino, Linxiao Zhu, Dakotah Thompson, Rohith Mittapally, and Pramod Reddy. Nanogap near-field thermophotovoltaics. *Nature Nanotechnology*, 13:806–811, 2018.

[27] Biswajeet Guha, Clayton Otey, Carl B. Poitras, Shanhui Fan, and Michal Lipson. Near-field radiative cooling of nanostructures. *Nano Letters*, 12(9):4546–4550, August 2012.

[28] X.L. Liu, R.Z. Zhang, and Z.M. Zhang. Near-field radiative heat transfer with doped-silicon nanostructured metamaterials. *International Journal of Heat and Mass Transfer*, 73:389–398, June 2014.

[29] Linxiao Zhu, Anthony Fiorino, Dakotah Thompson, Rohith Mittapally, and Edgar Meyhofer. Near-field photonic cooling through control of the chemical potential of photons. *Nature*, 566:239–244, 2019.

[30] Yanpei Tian Fangqi Chen, Xiaojie Liu and Yi Zheng. Dynamic tuning of near-field radiative thermal rectification. *Advanced Engineering Materials*, 23(2):2000825, 2021.

[31] Lei Tang, John DeSutter, and Mathieu Francoeur. Near-field radiative heat transfer between dissimilar materials mediated by coupled surface phonon- and plasmon-polaritons. *ACS Photonics*, 7(5):1304–1311, April 2020.

[32] Mikyung Lim, Jaeman Song, Seung S. Lee, and Bong Jae Lee. Tailoring near-field thermal radiation between metallo-dielectric multilayers using coupled surface plasmon polaritons. *Nature Communications*, 9(1), October 2018.

[33] Mathieu Francoeur, M. Pinar Menguc, and Rodolphe Vaillon. Near-field radiative heat transfer enhancement via surface phonon polaritons coupling in thin films. *Applied Physics Letters*, 93(4):043109, July 2008.

[34] Karl Joulain, Jeremie Drevillon, and Philippe Ben-Abdallah. Noncontact heat transfer between two metamaterials. *Physical Review B*, 81(16), April 2010.

[35] Jinlin Song, Qiang Cheng, Lu Lu, Bowen Li, Kun Zhou, Bo. Zhang, Zixue Luo, and Xinping Zhou. Magnetically tunable near-field radiative heat transfer in hyperbolic metamaterials. *Phys. Rev. Applied*, 13:024054, Feb 2020.

[36] V. Fernandez-Hurtado, F.J. Garcia-Vidal, Shanhui Fan, and J.C. Cuevas. Enhancing near-field radiative heat transfer with si-based metasurfaces. *Physical Review Letters*, 118(20), May 2017.

[37] X. L. Liu and Z. M. Zhang. Graphene-assisted near-field radiative heat transfer between corrugated polar materials. *Applied Physics Letters*, 104(25):251911, June 2014.

[38] Haifeng Liang. Mid-infrared response of reduced graphene oxide and its high-temperature coefficient of resistance. *AIP Advances*, 4(10):107131, October 2014.

[39] Chucai Guo, Jianfa Zhang, Wei Xu, Ken Liu, Xiaodong Yuan, Shiqiao Qin, and Zhihong Zhu. Graphene-based perfect absorption structures in the visible to terahertz band and their optoelectronics applications. *Nanomaterials*, 8(12):1033, December 2018.

[40] Yaser Hajati. Tunable broadband multiresonance graphene terahertz sensor. *Optical Materials*, 101:109725, March 2020.

[41] K. S. Novoselov. Electric field effect in atomically thin carbon films. *Science*, 306(5696):666–669, October 2004.

[42] R. R. Nair, P. Blake, A. N. Grigorenko, K. S. Novoselov, T. J. Booth, T. Stauber, N. M. R. Peres, and A. K. Geim. Fine structure constant defines visual transparency of graphene. *Science*, 320(5881):1308–1308, June 2008.

[43] A. Vakil and N. Engheta. Transformation optics using graphene. *Science*, 332(6035):1291–1294, June 2011.

[44] Yu Yao, Mikhail A. Kats, Raji Shankar, Yi Song, Jing Kong, Marko Loncar, and Federico Capasso. Wide wavelength tuning of optical antennas on graphene with nanosecond response time. *Nano Letters*, 14(1):214–219, December 2013.

[45] T.J. Echtermeyer, L. Britnell, P.K. Jasnos, A. Lombardo, R.V. Gorbachev, A.N. Grigorenko, A.K. Geim, A.C. Ferrari, and K.S. Novoselov. Strong plasmonic enhancement of photovoltage in graphene. *Nature Communications*, 2(1), August 2011.

[46] Riccardo Messina and Philippe Ben-Abdallah. Graphene-based photovoltaic cells for near-field thermal energy conversion. *Scientific Reports*, 3(1), March 2013.

[47] Junbo Wu, Mukul Agrawal, Hector A. Becerril, Zhenan Bao, Zunfeng Liu, Yongsheng Chen, and Peter Peumans. Organic light-emitting diodes on solution-processed graphene transparent electrodes. *ACS Nano*, 4(1):43–48, November 2009.

[48] Frank H. L. Koppens, Darrick E. Chang, and F. Javier Garcia de Abajo. Graphene plasmonics: A platform for strong light–matter interactions. *Nano Letters*, 11(8):3370–3377, August 2011.

[49] K. S. Novoselov, A. K. Geim, S. V. Morozov, D. Jiang, M. I. Katsnelson, I. V. Grigorieva, S. V. Dubonos, and A. A. Firsov. Two-dimensional gas of massless dirac fermions in graphene. *Nature*, 438(7065):197–200, November 2005.

[50] A. N. Grigorenko, M. Polini, and K. S. Novoselov. Graphene plasmonics. *Nature Photonics*, 6(11):749–758, November 2012.

[51] L A Falkovsky. Optical properties of graphene. *Journal of Physics: Conference Series*, 129:012004, October 2008.

[52] L. A. Falkovsky and S. S. Pershoguba. Optical far-infrared properties of a graphene monolayer and multilayer. *Physical Review B*, 76(15), October 2007.

[53] Ognjen Ilic, Marinko Jablan, John D. Joannopoulos, Ivan Celanovic, and Marin Soljacic. Overcoming the black body limit in plasmonic and graphene near-field thermophotovoltaic systems. *Optics Express*, 20(S3):A366, March 2012.

[54] George W. Hanson. Dyadic green's functions and guided surface waves for a surface conductivity model of graphene. *Journal of Applied Physics*, 103(6):064302, March 2008.

[55] Marcus Freitag, Hsin-Ying Chiu, Mathias Steiner, Vasili Perebeinos, and Phaedon Avouris. Thermal infrared emission from biased graphene. *Nature Nanotechnology*, 5(7):497–501, May 2010.

[56] Ognjen Ilic, Marinko Jablan, John D. Joannopoulos, Ivan Celanovic, Hrvoje Buljan, and Marin Soljacic. Near-field thermal radiation transfer controlled by plasmons in graphene. *Physical Review B*, 85(15), April 2012.

[57] Ge Yin, Jiang Yang, and Yungui Ma. Near-field heat transfer between graphene monolayers: Dispersion relation and parametric analysis. *Applied Physics Express*, 9(12):122001, November 2016.

[58] V. B. Svetovoy, P. J. van Zwol, and J. Chevrier. Plasmon enhanced near-field radiative heat transfer for graphene covered dielectrics. *Physical Review B*, 85(15), April 2012.

[59] Ognjen Ilic, Nathan H. Thomas, Thomas Christensen, Michelle C. Sherrott, Marin Soljacic, Austin J. Minnich, Owen D. Miller, and Harry A. Atwater. Active radiative thermal switching with graphene plasmon resonators. *ACS Nano*, 12(3):2474–2481, March 2018.

[60] Tobias Wenger, Giovanni Viola, Mikael Fogelstrom, Philippe Tassin, and Jari Kinaret. Optical signatures of nonlocal plasmons in graphene. *Physical Review B*, 94(20), November 2016.

[61] M R Ramezanali, M M Vazifeh, Reza Asgari, Marco Polini, and A H MacDonald. Finite-temperature screening and the specific heat of doped graphene sheets. *Journal of Physics A: Mathematical and Theoretical*, 42(21):214015, May 2009.

[62] Xiao Lin, Nicholas Rivera, Josue J Lopez, Ido Kaminer, Hongsheng Chen, and Marin Soljacic. Tailoring the energy distribution and loss of 2d plasmons. *New Journal of Physics*, 18(10):105007, October 2016.

[63] L. Frechette P. Ben-Abdallah, A. Belarouci and S.A. Biehs. Heat flux splitter for near-field thermal radiation. *Applied Physics Letters*, 107(5):053109, 2015.

[64] Ali Farmani, Abbas Zarifkar, Mohammad H.Sheikhi, and Mehdi Miri. Design of a tunable graphene plasmonic-on-white graphene switch at infrared range. *Superlattices and Microstructures*, 112:404–414, 2017.

[65] Riccardo Messina, Philippe Ben-Abdallah, Brahim Guizal, and Mauro Antezza. Graphene-based amplification and tuning of near-field radiative heat transfer between dissimilar polar materials. *Physical Review B*, 96(4), July 2017.

[66] Georgia T. Papadakis, Bo Zhao, Siddharth Buddhiraju, and Shanhui Fan. Gate-tunable near-field heat transfer. *ACS Photonics*, 6(3):709–719, 2019.

[67] Alejandro Manjavacas Renwen Yu and F. Javier García de Abajo. Ultrafast radiative heat transfer. *Nature communication*, 8(2), February 2017.

[68] Hugh O. H. Churchillab Desalegn T. Debu, M. Hasan Doha and Joseph B. Herzog. Gate voltage and doping effects on near-field radiation heat transfer in plasmonic heterogeneous pairs of graphene and black phosphorene. *RSC Adv.*, 9:29173–29181, 2019.

[69] Gang Zhang Jiebin Peng and Baowen Li. Thermal management in mos2 based integrated device using near-field radiation. *Applied Physics Letters*, 107(13):133108, 2015.

[70] Xiao-Jie Yi, Xiao-Juan Hong, Khurram Shehzad, Tong-Biao Wang, Xu-Ming Xu, Tian-Bao Yu Qing-Hua Liao, and Nian-Hua Liu. Near-field radiative heat transfer between black phosphorus and graphene sheet. *Materials Research Express*, 6(2):025906, nov 2018.

[71] A. I. Volokitin and B. N. J. Persson. Near-field radiative heat transfer between closely spaced graphene and amorphous sio_2. *Phys. Rev. B*, 83:241407, Jun 2011.

[72] Victor Fernandez-Hurtado, Antonio I. Fernandez-Dominguez, Johannes Feist, Francisco J. Garcia-Vidal, and Juan Carlos Cuevas. Exploring the limits of super-planckian far-field radiative heat transfer using 2d materials. *ACS Photonics*, 5(8):3082–3088, 2018.

[73] J. Song, Q. Cheng, and Huaichun Zhou. Near-field radiative heat transfer between graphene-covered anisotropic magneto-dielectric hyperbolic materials. In *Near-field radiative heat transfer between graphene-covered anisotropic magneto-dielectric hyperbolic materials*, 2016.

[74] B N J Persson and H Ueba. Heat transfer between graphene and amorphous sio_2. *Journal of Physics: Condensed Matter*, 22(46):462201, oct 2010.

[75] V P Gusynin, S G Sharapov, and J P Carbotte. Magneto-optical conductivity in graphene. *Journal of Physics: Condensed Matter*, 19(2):026222, December 2006.

[76] Lixin Ge, Ke Gong, Yuping Cang, Yongsong Luo, Xi Shi, and Ying Wu. Magnetically tunable multiband near-field radiative heat transfer between two graphene sheets. *Phys. Rev. B*, 100:035414, Jul 2019.

[77] Longji Cui Huihai Wu, Yong Huang and Keyong Zhu. Active magneto-optical control of near-field radiative heat transfer between graphene sheets. *Phys. Rev. Applied*, 11:054020, May 2019.

[78] Rong Cheng, Yuxiu Zhou, Hongfei Liu, Jianqiang Liu, Guanghou Sun, Xueyun Zhou, Hong Shen, Qingkai Wang, and Yikun Zha. Tunable graphene-based terahertz absorber via an external magnetic field. *Opt. Mater. Express*, 10(2):501–512, Feb 2020.

[79] Lixin Ge, Zijun Xu, Yuping Cang, and Ke Gong. Modulation of near-field radiative heat transfer between graphene sheets by strain engineering. *Opt. Express*, 27(16):A1109–A1117, aug 2019.

[80] Yi-Fan Liao and Guo-You Wang. Active control of near-field radiative heat transfer via multiple coupling of surface waves with graphene plasmon. *Eur. Phys. J. B*, 92(65), 2019.

[81] Fanglin Bao Kezhang Shi and Sailing He. Enhanced near-field thermal radiation based on multilayer graphene-hbn heterostructures. *ACS Photonics*, 4(4), 2017.

[82] Jinlin Song and Qiang Cheng. Near-field radiative heat transfer between graphene and anisotropic magneto-dielectric hyperbolic metamaterials. *Physical Review B*, 94(12), September 2016.

[83] B. Zhao and Z.M. Zhang. Enhanced Photon Tunneling by Surface Plasmon–Phonon Polaritons in Graphene/hBN Heterostructures. *Journal of Heat Transfer*, 139(2), feb 2017.

[84] Liang-Ying Zhong, Qi-Mei Zhao, Tong-Biao Wang, Tian-Bao Yu, Qing-Hua Liao, and Nian-Hua Liu. Near-field radiative heat transfer between graphene/silicon carbide multilayers. *Journal of Heat Transfer*, 140(7), April 2018.

[85] Xiao-Juan Hong, Tong-Biao Wang, De-Jian Zhang, Wen-Xing Liu, Tian-Bao Yu, Qing-Hua Liao, and Nian-Hua Liu. The near-field radiative heat transfer between graphene/SiC/hBN multilayer structures. *Materials Research Express*, 5(7):075002, jul 2018.

[86] Zhiheng Zheng, Ao Wang, and Yimin Xuan. Spectral tuning of near-field radiative heat transfer by graphene-covered metasurfaces. *Journal of Quantitative Spectroscopy and Radiative Transfer*, 208:86–95, 2018.

[87] Ming-Jian He, Hong Qi, Yi-Fei Wang, Ya-Tao Ren, Wei-Hua Cai, and Li-Ming Ruan. Near-field radiative heat transfer in multilayered graphene system considering equilibrium temperature distribution. *Opt. Express*, 27(16):953–966, aug 2019.

[88] Yong Zhang, Cun-Hai Wang, Hong-Liang Yi, and He-Ping Tan. Multiple surface plasmon polaritons mediated near-field radiative heat transfer between graphene/vacuum multilayers. *Journal of Quantitative Spectroscopy and Radiative Transfer*, 221:138–146, 2018.

[89] P. J. van Zwol, S. Thiele, C. Berger, W. A. de Heer, and J. Chevrier. Nanoscale radiative heat flow due to surface plasmons in graphene and doped silicon. *Phys. Rev. Lett.*, 109:264301, Dec 2012.

[90] Jiang Yang, Wei Du, Yishu Su, Yang Fu, Shaoxiang Gong, Sailing He, and Yungui Ma. Observing of the super-planckian near-field thermal radiation between graphene sheets. *Nature Communications*, 9:4033, October 2018.

[91] Nathan H. Thomas, Michelle C. Sherrott, Jeremy Broulliet, Harry A. Atwater, and Austin J. Minnich. Electronic modulation of near-field radiative transfer in graphene field effect heterostructures. *Nano Letters*, 19(6):3898–3904, 2019.

[92] Z. Q. Li, E. A. Henriksen, Z. Jiang, Z. Hao, M. C. Martin, P. Kim, H. L. Stormer, and D. N. Basov. Dirac charge dynamics in graphene by infrared spectroscopy. *Nature Physics*, 4:532–532, June 2008.

[93] Mathieu Francoeur and M. Pinar Mengüç. Role of fluctuational electrodynamics in near-field radiative heat transfer. *Journal of Quantitative Spectroscopy and Radiative Transfer*, 109(2):280–293, 2008. The Fifth International Symposium on Radiative Transfer.

[94] Gerhard Kristensson. *Scattering of Electromagnetic Waves by Obstacles*. Electromagnetic Waves. Institution of Engineering and Technology, 2016.

[95] Zhuomin M. Zhang. *Nano/microscale heat transfer*. Springer, 2 edition, 2020.

[96] Sergei M. Rytov, Yurii A. Kravtsov, and Valeryan I. Tatarskii. *Principles of statistical radiophysics 3: elements of random fields*. Springer, 2012.

[97] J. Lussange, R. Guerout, F. S. S. Rosa, J. Greffet, A. Lambrecht, and S. Reynaud. Radiative heat transfer between two dielectric nanogratings in the scattering approach. *Physical Review B*, 86(8), August 2012.

[98] L. Tsang, J.A. Kong, and K.H. Ding. *Scattering of Electromagnetic Waves: Theories and Applications*. Wiley Series in Remote Sensing and Image Processing. Wiley, 2004.

[99] Mathieu Francoeur, M. Pinar Mengüç, and Rodolphe Vaillon. Solution of near-field thermal radiation in one-dimensional layered media using dyadic green's functions and the scattering matrix method. *Journal of Quantitative Spectroscopy and Radiative Transfer*, 110(18):2002–2018, 2009.

[100] C.J. Fu and Z.M. Zhang. Nanoscale radiation heat transfer for silicon at different doping levels. *International Journal of Heat and Mass Transfer*, 49(9):1703–1718, 2006.

[101] John DeSutter, Lei Tang, and Mathieu Francoeur. A near-field radiative heat transfer device. *Nature Nanotechnology*, 14(8):751–755, July 2019.

[102] Yong Zhang, Cheng-Long Zhou, Lei Qu, and Hong-Liang Yi. Active control of near-field radiative heat transfer through nonreciprocal graphene surface plasmons. *Applied Physics Letters*, 116(15):151101, April 2020.

[103] A. Narayanaswamy and G. Chen. Direct computation of thermal emission from nanostructures. *Annual Review of Heat Transfer*, 14:169–195, 2005.

[104] Mathieu Francoeur, M Pinar Menguc, and Rodolphe Vaillon. Spectral tuning of near-field radiative heat flux between two thin silicon carbide films. *Journal of Physics D: Applied Physics*, 43(7):075501, February 2010.

[105] Riccardo Messina, Jean-Paul Hugonin, Jean-Jacques Greffet, Fran çois Marquier, Yannick De Wilde, Ali Belarouci, Luc Frechette, Yvon Cordier, and Philippe Ben-Abdallah. Tuning the electromagnetic local density of states in graphene-covered systems via strong coupling with graphene plasmons. *Phys. Rev. B*, 87:085421, Feb 2013.

[106] P. A. D. Goncalves and N. M. R. Peres. *An Introduction to Graphene Plasmonics*. WORLD SCIENTIFIC, December 2015.

[107] Zoltán Mics, Klaas-Jan Tielrooij, Khaled Parvez, Søren A. Jensen, Ivan Ivanov, Xinliang Feng, Klaus Mullen, Mischa Bonn, and Dmitry Turchinovich. Thermodynamic picture of ultrafast charge transport in graphene. *Nature Communications*, 6(1), July 2015.

[108] Pochi Yeh. *Optical Waves in Layered Media*. Wiley, 2005.

[109] Neil W. Ashcroft and N. David Mermin. *Solid state physics*. Philadelphia, Pa. : Saunders college, 1976.

[110] Jahan M. Dawlaty, Shriram Shivaraman, Jared Strait, Paul George, Mvs Chandrashekhar, Farhan Rana, Michael G. Spencer, Dmitry Veksler, and Yunqing Chen. Measurement of the optical absorption spectra of epitaxial graphene from terahertz to visible. *Applied Physics Letters*, 93(13):131905, September 2008.

[111] E. H. Hwang and S. Das Sarma. Dielectric function, screening, and plasmons in two-dimensional graphene. *Physical Review B*, 75(20), May 2007.

[112] Zhuomin M. Zhang and Hong Ye. Measurements of radiative properties of engineered micro nanostructures. *Annual Review of Heat Transfer*, 16(1):345–396, 2013.

[113] E. Ozbay. Plasmonics: Merging photonics and electronics at nanoscale dimensions. *Science*, 311(5758):189–193, January 2006.

[114] H. F. Ghaemi, Tineke Thio, D. E. Grupp, T. W. Ebbesen, and H. J. Lezec. Surface plasmons enhance optical transmission through subwavelength holes. *Physical Review B*, 58(11):6779–6782, September 1998.

[115] Yu-Bin Chen and Chien-Jing Chen. Interaction between the magnetic polariton and surface plasmon polariton. *Optics Communications*, 297:169–175, June 2013.

[116] A. V. Krasavin and A. V. Zayats. Passive photonic elements based on dielectric-loaded surface plasmon polariton waveguides. *Applied Physics Letters*, 90(21):211101, May 2007.

[117] R. Gupta, M. J. Dyer, and W. A. Weimer. Preparation and characterization of surface plasmon resonance tunable gold and silver films. *Journal of Applied Physics*, 92(9):5264–5271, November 2002.

[118] Venu Gopal Achanta. Surface waves at metal-dielectric interfaces: Material science perspective. *Reviews in Physics*, 5:100041, 2020.

[119] A. H. Castro Neto, F. Guinea, N. M. R. Peres, K. S. Novoselov, and A. K. Geim. The electronic properties of graphene. *Reviews of Modern Physics*, 81(1):109–162, January 2009.

[120] Zheyu Fang, Yumin Wang, Zheng Liu, Andrea Schlather, Pulickel M. Ajayan, Frank H. L. Koppens, Peter Nordlander, and Naomi J. Halas. Plasmon-induced doping of graphene. *ACS Nano*, 6(11):10222–10228, September 2012.

[121] Long Ju, Baisong Geng, Jason Horng, Caglar Girit, Michael Martin, Zhao Hao, Hans A. Bechtel, Xiaogan Liang, Alex Zettl, Y. Ron Shen, and Feng Wang. Graphene plasmonics for tunable terahertz metamaterials. *Nature Nanotechnology*, 6(10):630–634, September 2011.

[122] Hugen Yan, Xuesong Li, Bhupesh Chandra, George Tulevski, Yanqing Wu, Marcus Freitag, Wenjuan Zhu, Phaedon Avouris, and Fengnian Xia. Tunable infrared plasmonic devices using graphene/insulator stacks. *Nature Nanotechnology*, 7(5):330–334, April 2012.

[123] Xiao Yong He and Rui Li. Comparison of graphene-based transverse magnetic and electric surface plasmon modes. *IEEE Journal of Selected Topics in Quantum Electronics*, 20(1):62–67, 2014.

[124] Adam Mock. Pade approximant spectral fit for FDTD simulation of graphene in the near infrared. *Optical Materials Express*, 2(6):771, May 2012.

APPENDIX A

MATLAB CODES

A.1 MATLAB code for NFRHT

```
clear all
clc

global eps1 eps2 eps3 w D iw T1 T3 muc Sigma1 Sigma3

%Constants
hbar = 1.05457173e-34;
Kb = 1.3806488e-23;
ev = 1.60217646e-19;


%Problem geometry

D = 10e-9; % equal to dc which is the gap between media 1 and 3
T1 = 300;
T3 = 290;
muc = 0.5*ev;  %chemical potential of graphene in eV

ww = linspace(5e11,5e14,200);
Nw = length(ww);

QP = 0;
QE = 0;
```

```
24 Q(1:Nw) = 0;
25
26
27 for iw = 1:Nw
28     iw
29     w = ww(iw);
30
31     Sigma1 = Kubo( muc,T1 );
32     Sigma3 = Kubo( muc,T3 );
33
34     eps1 = 1.0;
35     eps2 = 1.0;
36     eps3 = 1.0;
37
38     %Theta
39     theta1 = hbar*w/(exp((hbar*w)/(Kb*T1))-1);
40     theta3 = hbar*w/(exp((hbar*w)/(Kb*T3))-1);
41     theta = theta1-theta3;
42
43     %Wavevectors
44     k2 = w/2.998e8; %kv
45
46     %Integraton of the propagating waves
47     Integ = quadgk(@Z_P_v2,0,k2-1e-6);
48     QP = theta/(4*pi^2)*Integ;
49
50     %defining a waypoint
```

```
51      cc = logspace(8,15,10);
52      co = cc.*k2;
53
54      %Integraton of the evaneent waves
55      Integ = quadgk(@Z_E_v2,k2+1e-4,inf,'waypoint',co,'RelTol',1e-6);
56      QE = theta/(4*pi^2)*Integ;
57
58      Q(iw) = QP+QE;
59  end
60
61  Q_total = trapz(ww,Q);
```

A.2 MATLAB code for radiative conductance

```
1  clear all
2  clc
3
4  global eps1 eps2 eps3 w D iw T muc Sigma
5
6  %Constants
7  hbar = 1.05457173e-34;
8  Kb = 1.3806488e-23;
9  ev = 1.60217646e-19;
10
11
12 %Problem geometry
13
14 D = 50e-9; % equal to dc which is the gap between media 1 and 3
```

```
15
16 T = 800;
17 muc = 0.2*ev;
18 ww = linspace(5e11,5e14,200);
19
20 Nw = length(ww);
21 eps1 = 1.0;
22 eps2 = 1.0;
23 eps3 = eps1;
24
25 QP = 0;
26 QE = 0;
27
28
29 for iw = 1:Nw
30     iw
31
32     w = ww(iw);
33
34     Sigma = Kubo( muc,T );
35
36     %Differentiation of Theta
37     theta = hbar*w/(exp((hbar*w)/(Kb*T))-1);
38     theta = theta.^2.*exp(hbar*w./Kb./T)./(Kb*T^2);
39
40     %Wavevectors
41     k2 = w/2.998e8; %kv
```

```
42
43      %Integraton of the propagating waves
44      Integ = quadgk(@Z_P_v2,0,k2-1e-6);
45      QP = theta/(4*pi^2)*Integ;
46
47      %Defining a waypoint
48      cc = logspace(1,10,10);
49      co = cc.*k2;
50
51      %Integraton of the evaneent waves
52      Integ = quadgk(@Z_E_v2,k2+1e-4,inf,'waypoint',co,'RelTol',1e-6);
53      QE = theta/(4*pi^2)*Integ;
54
55      Q(iw) = QP+QE;
56
57  end
```

A.3 MATLAB code for Dispersion Relation

```
1  clear all
2  clc
3
4  global w D iw T1 muc k0 eps1 eps3 S3
5
6  %Constants
7  hbar = 1.05457173e-34;
8  Kb = 1.3806488e-23;
9  ev = 1.60217646e-19;
```

```
10 e0 = 8.8542e-12;                % Vacuum permittivity
11 eps1 = 1;
12 eps3 = 1;
13
14 %Problem geometry
15
16 D = 50e-9; % equal to dc which is the gap between media 1 and 3
17 T1 = 300;    %temperatue
18 c0 = 299792458; %Speed of light in vacuum (m/s)
19 muc = 0.0*ev;  %chemical potential of graphene in eV
20 nuf =c0/300;     %Fermi velocity
21
22 ww = linspace(5e11,5e14,20);
23 Nw = length(ww);
24
25 for iw = 1:Nw
26     iw
27     w = ww(iw);
28     k0 = w/2.998e8; %kv
29     k00(iw)=k0;
30
31     S3 = Kubo( muc,T1 );
32
33     %first solution
34     f1 = @(x) func(x);
35     %second solution
36     f2 = @(x) func2(x);
```

```
37      % Solution from the general formula
38      f = @(x) func3(x);
39
40      x1 = fminbnd(f1,0,400*k0);
41      x2 = fminbnd(f2,0,400*k0);
42      x3 = fminbnd(f,0,400*k0);
43
44      answer1(iw) = x1/k0;
45      answer2(iw) = x2/k0;
46      answer3(iw) = x3/k0;
47  end
```

A.4 MATLAB code for propagating exchange function

```
1  function [ ZP ] = Z_P_v2( krho )
2  global w D T muc Sigma1
3
4  e0 = 8.8542e-12;                % Vacuum permittivity
5  m0 = 1.25663706143592D-06;      % Vacuum permeability
6
7  Sigma1 = RPA( muc,krho,T );
8
9  %Wavevectors
10      k2 = w/2.998e8;
11
12 %Calculating kzs
13      kz2 = sqrt(k2^2-krho.^2);
14
```

```
%Fresnel reflection coefficients
% In TE polarization
r21TE = -(2*kz2./(Sigma1.*m0.*w)+1).^(-1);
t21TE = (1+m0.*w.*Sigma1./2./kz2).^(-1);

% IN TM polarization
r21TM = (2*e0*w./(Sigma1.*kz2)+1).^(-1);
t21TM = (1+Sigma1.*kz2./w./2./e0).^(-1);

%Exchange factors
ZP_TE = (1-abs(r21TE).^2-abs(t21TE).^2).^2./
                (abs(1-r21TE.^2.*exp(2i.*kz2*D))).^2);
ZP_TM = (1-abs(r21TM).^2-abs(t21TM).^2).^2./
                (abs(1-r21TM.^2.*exp(2i.*kz2*D))).^2);
ZP=(ZP_TE+ZP_TM).*krho;

end
```

A.5 MATLAB code for evanescent exchange function

```
function [ ZE ] = Z_E_v2( krho )
global w D T muc Sigma1

e0 = 8.8542e-12;                % Vacuum permittivity
m0 = 1.25663706143592D-06;  % Vacuum permeability

Sigma1 = RPA( muc,krho,T );

```

```
 %Wavevectors
      k2 = w/2.998e8;
%Calculating kzs
      kz2 = sqrt(k2.^2-krho.^2);


%Fresnel reflection coefficients
% In TE polarization
r21TE = -(2*kz2./(Sigma1.*m0.*w)+1).^(-1);

% IN TM polarization
r21TM = (2*e0*w./(Sigma1.*kz2)+1).^(-1);

%Exchange factors
ZE_TE = 4.*imag(r21TE).^2.*exp(-2.*imag(kz2)*D)./
                    (abs(1-r21TE.^2.*exp(-2.*imag(kz2)*D)).^2);
ZE_TM = 4.*imag(r21TM).^2.*exp(-2.*imag(kz2)*D)./
                    (abs(1-r21TM.^2.*exp(-2.*imag(kz2)*D)).^2);
ZE=(ZE_TE+ZE_TM).*krho;
end
```

A.6 MATLAB code for RPA

```
function [ Sigma_RPA ] = RPA( muc,krho,T )

global w

% constant
```

```
6  hbar = 1.054571817e-34;       % Planck's constant in J.s
7  KB = 1.380649e-23;            % Boltzmann constant (J/K)
8  c0 = 299792458;               % Speed of light in vacuum (m/s)
9  e_charge = 1.602176634e-19; % electron charge (C)
10
11 nuf = c0/300;                 %Fermi velocity (m/s) from "An Introduction
12                               %to graphene plasmonics", Page 32
13 alpha = [1,-1];               % Alpha
14
15     [Chi_re,Chi_im]=deal(0,0);
16
17 for i = 1:length(alpha)
18
19     C1 = heaviside(hbar.*nuf.*krho-hbar.*w).*krho.^2./
20                                   (2*hbar*sqrt((nuf.*krho).^2-(w).^2));
21     C2 = heaviside(hbar.*w-hbar.*nuf.*krho).*krho.^2./
22                                   (2*hbar*sqrt((w).^2-(nuf.*krho).^2));
23     if (T == 0 )
24         if ( alpha(i) == 1)
25             C3 = -2.*alpha(2).*muc./(hbar.*nuf).^2;
26         else
27             C3 = 0;
28         end
29     else
30         C3 = -2.*KB.*T.*log(1+exp(alpha(i).*muc./KB./T))
31                                   ./(hbar.*nuf).^2;
32     end
```

```
33
34      delta = (abs(alpha(i))-alpha(i))./2;
35
36          GP_func =@(x) G(alpha(i),krho,x,1,w,T,muc,nuf);
37          GM_func =@(x) G(alpha(i),krho,x,-1,w,T,muc,nuf);
38          HP_func =@(x) D(alpha(i),krho,x,1,w,T,muc,nuf);
39          HM_func =@(x) D(alpha(i),krho,x,-1,w,T,muc,nuf);
40
41      Chi_im = Chi_im +(C1.*(integral(GP_func,1,inf,'ArrayValued', true)
42              -integral(GM_func,1,inf,'ArrayValued', true))
43              +C2.*(-pi./2.*delta +integral(HP_func,-1,1,'ArrayValued', true)))
44
45      Chi_re = Chi_re +(C2.*(integral(GM_func,1,inf,'ArrayValued', true)
46              -integral(GP_func,1,inf,'ArrayValued', true))
47              +C1.*(-pi./2.*delta +integral(HM_func,-1,1,'ArrayValued', true)))
48      Chi_re = Chi_re + (C3./pi);
49  end
50      Sigma_RPA = 1i*e_charge^2*w*
51                              (Chi_re + 1i.*Chi_im)./krho.^2;
52  end
```

A.7 MATLAB code for functions used in RPA

```
1  function [ f ] = H(alpha,x,krho,fsign,w,T,muc)
2
3  hbar = 1.054571817e-34;       % plancks contant in J.s
4  KB = 1.380649e-23;            % Boltzmann constant (J/K)
5  nuf = 1e6;                        % fermi velocity (m/s)
```

```
6
7  f = sqrt(1 - x.^2)./(exp((hbar*abs(nuf.*krho.*x+fsign.*w)
8                                  -2.*alpha.*muc)./2./KB./T)+1);
9  end
```

```
1  function [ f ] = G(alpha,krho,x,fsign,w,T,muc,nuf)
2
3  hbar = 1.054571817e-34;        % plancks contant in J.s
4  KB = 1.380649e-23;             % Boltzmann constant (J/K)
5
6  f = sqrt(x.^2 -1)./(exp((abs(hbar.*nuf.*krho.*x+fsign.*hbar.*w)
7                                  -2.*alpha.*muc)./(2*KB*T))+1);
8  end
```

```
1  function [ f ] = D(alpha,krho,x,fsign,w,T,muc,nuf)
2
3  hbar = 1.054571817e-34;        % plancks contant in J.s
4  KB = 1.380649e-23;             % Boltzmann constant (J/K)
5
6  f = sqrt(1 - x.^2)./(exp((abs(hbar.*nuf.*krho.*x+fsign.*hbar.*w)
7                                  -2.*alpha.*muc)./(2*KB*T))+1);
8  end
```

A.8 MATLAB code for Kubo

```
1  function [ Sigma_Kubo ] = Kubo( EF,T )
2
3  global w
4
```

```
% constant
hbar = 1.054571817e-34;       % plancks contant in J.s
KB = 1.380649e-23;            % Boltzmann constant J/K
eV = 1.60218e-19;             % eV to J, and electron charge in C
tau = 1e-13;                  % Add reference

gamma = 1/tau; % 3.7e-3*eV/hbar;
sigma_0 = eV^2/(4*hbar);

    intra = 4/(pi*(hbar*gamma-1i*hbar*w))*
                            (EF+2*KB*T*log(1+exp(-EF/(KB*T))));
    func =@(x) (G2(x,T,EF)-G2(hbar.*w./2,T,EF))./
                                    ((hbar.*w).^2 - 4.*x.^2);
    inter1 = G2(hbar.*w./2,T,EF);
    integ = integral(func,0,Inf,'RelTol',1e-6,'ArrayValued', true);
    inter2 =  4i.*hbar.*w./pi.*integ;
    inter = inter1+inter2;

    Sigma_Kubo = sigma_0*(intra + inter);
end
```

A.9 MATLAB code for function used in Kubo

```
function [ f ] = G2(x,T,muc)
KB = 1.380649e-23;            % Boltzmann constant (J/K)

f = 1./(cosh(muc./KB./T)./sinh(x./KB./T)+coth(x./KB./T));
end
```

A.10 MATLAB code for functions used in Dispersion Relation

```
function f1 = func(krho)

global w D T1 muc S1 k0 eps1 eps3

    e0 = 8.8542e-12;              % Vacuum permittivity
    S1 = RPA( muc,krho,T1 );
    kz = sqrt(krho.^2-k0^2);

    f1 = abs(eps3./kz.*coth(kz*D./2)+eps1./kz+1i.*S1./w./e0);
end
```

```
function f2 = func2(krho)

global w D T1 muc S1 k0 eps1 eps3

    e0 = 8.8542e-12;              % Vacuum permittivity
    S1 = RPA( muc,krho,T1 );
    kz = sqrt(krho.^2-k0^2);

    f2 = abs(eps3./kz.*tanh(kz*D./2)+eps1./kz+1i.*S1./w./e0);
end
```

```
function f1 = func3(krho)

global w D S3 k0 eps1 eps3
    e0 = 8.8542e-12;              % Vacuum permittivity
    kz = sqrt(krho.^2-k0^2);
```

```
6       f1 = abs(eps3./kz.*coth(kz*D./2)+eps1./kz+1i.*S3./w./e0);
7   end
```

BIOGRAPHY OF THE AUTHOR

Born in Gilan Province of Iran. At early age, diagnosed with X-Linked Retinoschisis and meningioma which caused lost most of eyesight and many other problems. In 2008, attended the Gilan University as a BSc mechanical engineering student majoring in heat and fluids while working as a programmer and web developer to find the money for brain surgery. In spite of all these, managed to get my MSc in mechanical engineering from University of Zanjan. By overcoming these hardships, found a much more explicit purpose for life: to pull as many people alike out of the misery I, myself was stuck in.

Behrad Zeinali Tajani is a candidate for the Master of Science degree in Mechanical Engineering from the University of Maine in August 2021.